International Journal of Nanomedicine

Dovepress
Taylor & Francis Group

Open Access Full Text Article

ORIGINAL RESEARCH

Biomimetic Barium Titanate/PLA Scaffold with Shape Memory and Bioelectro-Active Capacities Promotes Bone Regeneration

Shiyan Lv[1,*], Yuechi Zhang[2,*], Xiongjie Liang[1,*], Wenbo Xu[1], Zhibin Geng[1], Weifeng Hu[1], Xiaoyan Wang[1], Helin Li[1], Wenhui Guo[1], Yongbin Jing[1], Xiaoqi Liu[1], Huichao Fu[1], Gongping Xu[1], Chunyang Xi[1], Jinglong Yan[1], Hui Chi[1]

[1]Department of Orthopedic Surgery, The Second Affiliated Hospital, Harbin Medical University, Harbin, 150086, People's Republic of China; [2]Department of Astronautical Science and Mechanics, Harbin Institute of Technology (HIT), Harbin, 150001, People's Republic of China

*These authors contributed equally to this work

Correspondence: Jinglong Yan; Hui Chi, Email yanjinglong2025@163.com; chihui2024@163.com

Background: Bone, a natural piezoelectric material, converts mechanical stress to electrical signals; local bioelectric changes in defects affect repair. Current biomimetic bone materials focus on composition, bioactivity and structure, neglecting bioelectric effects. Piezoelectric materials reconstruct electrical microenvironments, simulating natural regulation and addressing traditional materials' structural reliance, offering effective repair strategies.

Methods: In this study, barium titanate piezoelectric nanoceramic particles were embedded into thermoresponsive shape-memory polylactic acid via 4D printing to fabricate BT/PLA composite scaffolds. The scaffolds were characterized using scanning electron microscopy, X-ray diffraction, surface roughness analysis, water contact angle measurement, as well as mechanical and piezoelectric property tests. Cellular experiments were performed to verify the effects of these scaffolds on the proliferation, adhesion, and osteogenic capacity of bone marrow mesenchymal stem cells under low-intensity pulsed ultrasound stimulation. Additionally, a rat calvarial defect model was established to evaluate the in vivo bone repair efficacy of the scaffolds.

Results: A shape-memory piezoelectric BT/PLA scaffold was 4D-printed. The 20 wt% BT scaffold showed excellent mechanics (~25 MPa compressive strength) and shape memory (full recovery in 5s), meeting clinical needs. All scaffolds were non-cytotoxic; BT/PLA with LIPUS generated ~1 μA current, promoting BMSC proliferation and osteogenesis. BT/PLA + LIPUS showed superior in vivo bone formation in rats, validating clinical potential for critical defects.

Conclusion: The BT/PLA scaffold, combining shape-memory and piezoelectric effects, shows significant bone regeneration potential. Its degradability with 4D printing may facilitate translation of personalized bone repair implants from bench to bedside. Transcriptome sequencing suggests its osteogenic effect may involve the PI3K-Akt pathway, providing a basis for optimizing molecular targets in future bone regenerative materials and reinforcing the study's scientific value in material design and mechanistic exploration.

Keywords: 4D-printing, bone regeneration, electric stimulation, piezoelectric scaffolds, shape memory

Introduction

Clinically, addressing large segmental bone defects resulting from trauma, infection, tumors, or surgical interventions continues to pose significant challenges. Every year, millions of patients are disabled due to bone defects worldwide.[1–3] Biomaterials-based bone tissue engineering technologies have opened up a new way for bone repair.[4–6] Bone, as a natural piezoelectric material, possesses intrinsic piezoelectric properties that can convert mechanical stimuli into electrical signals. Studies have shown that electrical stimulation (ES) can modulate cell membrane potential, ion channels, and cellular activity, and has been demonstrated to enhance the osteogenic differentiation of various types of mesenchymal stem cells.[7–10] However, during bone injury, the physiological electro-microenvironment at the fracture site is disrupted,

Received: 17 March 2025
Accepted: 14 October 2025
Published: 31 October 2025

Graphical Abstract

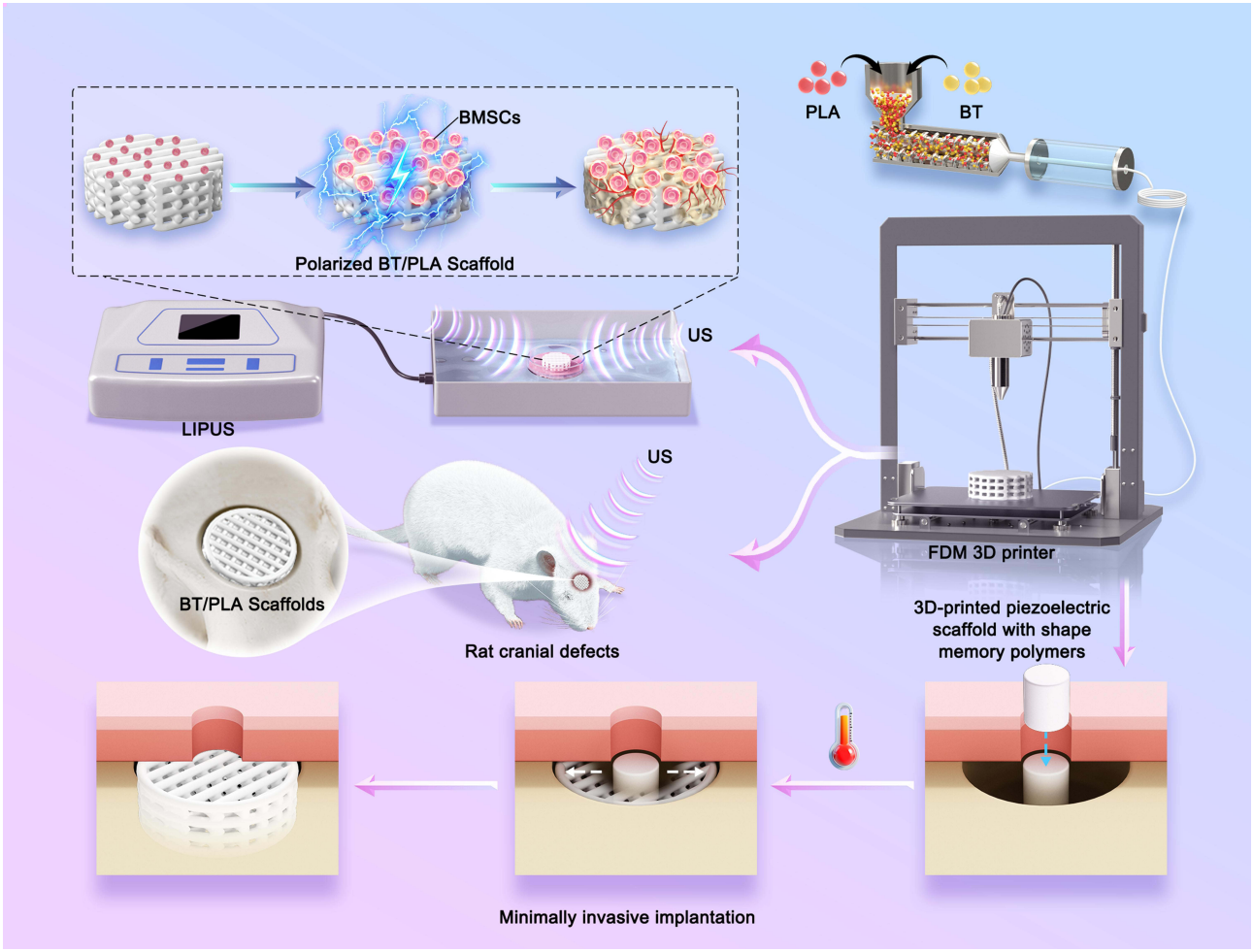

impairing the transmission of electrical charges and potentials across the fracture region.[11–14] Therefore, reconstructing the electrical microenvironment locally at the bone defect site through electroactive biomaterials can provide an effective strategy for promoting bone regeneration.

Among various piezoelectric materials, barium titanate (BT) nanoparticles exhibit excellent biocompatibility, bioactivity, and osteogenic potential.[15,16] Compared with polyvinylidene fluoride (PVDF), zinc oxide (ZnO), and poly-L-lactic acid (PLLA), it exhibits a higher piezoelectric coefficient (d33 = 191 pC/N) and lower dielectric loss, and can significantly improve the piezoelectric properties of composite materials, which has attracted extensive attention in the field of regenerative medicine.[17,18] By contrast, PVDF suffers from higher dielectric loss, rendering it difficult to maintain stable electrical signal output in long-term implantation applications. ZnO, conversely, poses a risk of excessive zinc ion release in physiological environments, which may suppress osteoblast activity.[19] However, as a piezoelectric ceramic, BT is characterized by mechanical brittleness and insufficient toughness. Therefore, the application of BT mainly depends on making it into a surface coating of bone implants or embedding it into polymers to construct BT/polymer composite materials, so as to endow the materials with mechanical stability and piezoelectricity and prevent the release of ions.[20–24]

In addition, the implantation of bone repair materials usually requires an open - surgery method, which will undoubtedly cause further damage to the local bone injury and aggravate the destruction of the bone regeneration micro- environment. Therefore, the development of minimally invasive implantation strategies for bone repair materials

remains a critical unmet need. Shape - memory - intelligent polymers (SMPs) are capable of undergoing reversible transformations between an initial memorized shape, a temporarily deformed state, and a restored original shape under specific conditions, such as temperature, UV light, or pH changes.[25–27] Therefore, utilizing the shape memory function of SMPs offers the potential for minimally invasive implantation of bone repair materials. Poly(lactic acid) (PLA), a biocompatible linear polymer, possesses advantages such as biocompatibility, biodegradability, good mechanical properties, and ease of processing. By adjusting the composition and content of the cross - linking agent, tributyl citrate (TBC), the molecular structure of PLA can be optimized. Through melt or solution blending, a cross - linked network structure can be formed, endowing the material with shape memory functionality.

In the context of piezoelectric scaffolds, 4D printing technology enables the precise integration of intelligent materials with shape-memory and piezoelectric properties, paving the way for new prospects in tissue engineering applications. Building upon traditional 3D printing, 4D printing introduces time as the fourth dimension, allowing fabricated structures to undergo preprogrammed deformations in response to external stimuli.[27] This technology enables the fabrication of complex stimuli-responsive architectures that can adapt to the dynamic microenvironment of biological systems, holding the promise to revolutionize the field of regenerative medicine.

For piezoelectric materials, mechanical force is required to activate their piezoelectric potential. However, in the early stage of bone repair, patients often need to be immobilized and cannot provide effective mechanical stimulation to the fracture site, which also increases the difficulty in the application of piezoelectric materials. Researchers have attempted to place the piezoelectric material in a high-voltage electric field for polarization before implanting it into the body. However, the results have proven that the polarization effect generated in this way will decay over time, showing significant dielectric loss. This makes it challenging to maintain a stable and sustained bioelectric microenvironment at the fracture site.[28,29] Low-intensity pulsed ultrasound (LIPUS) is a mechanical wave transmitted in the form of high-frequency pressure waves, with the advantages of being non-invasive, safe, effective, having controllable intensity parameters, and being easy to operate. As a gentle mechanical wave, LIPUS has been approved by the FDA as an adjunctive therapy to accelerate bone fracture healing.[30,31] Numerous studies have confirmed that dipoles within piezoelectric materials undergo deflection under low-frequency pulsed ultrasound, generating polarized charges to construct an electrical microenvironment for cell growth. Concurrently, this electrical microenvironment facilitates the activation of cellular signaling pathways, thereby promoting osteoblast proliferation and differentiation.[32] Therefore, using LIPUS as a mechanical driving method can enable the piezoelectric scaffold to exert a continuous and stable piezoelectric effect, which is expected to meet the requirements of minimally invasive implantation and reconstruction of the local electrical micro - environment at the fracture site simultaneously.

In summary, based on the concept of bone repair through reconstructing the local electrical microenvironment, this study employed barium titanate ($BaTiO_3$) nanoparticles as piezoelectric elements and low-intensity pulsed ultrasound (LIPUS) as the piezoelectric driving method to fabricate a $BaTiO_3$/PLA scaffold with both shape memory and piezoelectric properties via 4D printing technology. The surface properties of the $BaTiO_3$/PLA scaffold were characterized using scanning electron microscopy (SEM), transmission electron microscopy (TEM), X-ray diffraction (XRD), water contact angle measurement, and surface roughness analysis. Four experimental groups were then established for comparative analysis: pure polylactic acid (PLA), $BaTiO_3$/PLA composite, PLA + LIPUS, and $BaTiO_3$/PLA + LIPUS. In vitro proliferation and osteogenic differentiation of rat bone marrow mesenchymal stem cells (BMSCs) on the scaffolds were systematically evaluated. Additionally, the in vivo bone integration and osteogenesis properties were assessed using a calvarial defect model in Sprague-Dawley (SD) rats. Through comprehensive in vitro and in vivo experiments, this study systematically investigated the bone repair capacity and underlying osteogenic mechanisms of the scaffold, aiming to provide novel insights for the development of bone tissue engineering scaffolds and ultimately facilitate the rapid healing of patients with large-segment bone defects.

Materials and Methods

Preparation of BT/PLA Composite Printing Lines

Medical-grade polylactic acid (PLA, NatureWorks, USA, molecular weight of 100 kDa) pellets and barium titanate (BT, Aladdin) powder were pre-dried in a vacuum oven at 80°C for 4 hours prior to mixing. BT was incorporated into the PLA

matrix in mass fractions of 15%, 20%, 25%, and 30%, thoroughly mixed, and subsequently introduced into the hopper of a twin-screw extruder. The extrudates were water-cooled, drawn, and stretched into composite filaments.

Preparation of BT/PLA Composite Scaffolds

The scaffold geometry was designed using the commercial software SolidWorks. Subsequently, the BT/PLA composite scaffolds were fabricated via a fused deposition modeling (FDM) 3D printer (ANYCUBIC i3 MEGA) under the following parameters: a printing temperature of 200°C, a nozzle diameter of 0.4 mm, air cooling at 25°C, and a layer thickness of 0.2 mm. Three distinct types of specimens were printed: standard samples for mechanical testing, rectangular samples for shape memory and dynamic mechanical analysis, and porous scaffold samples for biological experiments.

Scaffold Characteristics

Shape Memory of the Scaffold

Dynamic mechanical analysis (DMA) is crucial for evaluating shape memory properties by determining the material's glass transition temperature. First, the rectangular specimen is immersed in 70°C hot water and deformed into a temporary shape by applying external force in the high-elastic state. The specimen is then cooled in cold water to fix the temporary shape, and once stabilized, the external force is removed, recording the bending angle as θ_0. The fixed specimen is subsequently re-immersed in a high-temperature water bath to recover its original shape, with the recovered angle recorded as θ_N. Finally, the shape memory performance is characterized by calculating the shape recovery ratio and comparing the recovery time.

The value of shape recovery rate is calculated as: $R_N = \frac{\theta_0 - \theta_N}{\theta_0} \times 100\%$.

Internal and Surface of the Scaffold

The scaffolds underwent a sputter-coating process with gold, followed by the examination of their structural morphology and surface characteristics using a scanning electron microscope (SEM; Tescan, Amber, Czech Republic). The analysis of elemental distribution and content within the composite scaffolds was performed using energy-dispersive X-ray spectroscopy (EDS). Furthermore, transmission electron microscopy (TEM, Talos F200X G2) was utilized to explore the microstructural morphology and crystalline structure of BT as well as BT/PLA nanoparticles.

Scaffold Mechanical Properties

To evaluate the mechanical properties of the composite scaffolds, compression tests were conducted at room temperature. Cylindrical specimens with a diameter of 10 mm and a height of 10 mm were used for the tests, and precise measurements were performed using a Zwick/Roell-010 universal testing machine at a loading rate of 2 mm/min.

Piezoelectric Properties of the Scaffold

The scaffolds underwent polarization for a duration of 30 minutes within an electric field of 4 kV/mm^{-1}. Subsequently, the d33 piezoelectric coefficient was assessed utilizing a quasi-static d33 meter (ZJ-3A). To simulate the mechanical stimulation, the scaffold was placed in an ultrasonic device. Samples were treated with low-intensity pulsed ultrasound (LIPUS) at a sine wave frequency of 1.0 MHz, utilizing a pulse repetition frequency of 1 kHz, an intensity level of 30 mW/cm², and a duty cycle set at 20%. The output current of the scaffold under low-frequency ultrasound was recorded using an electrometer.

XRD Analysis

The PLA, BT powders, and BT/PLA composite materials were analyzed using X-ray diffraction (XRD, MiniFlex600, Japan) at a scanning rate of 2°/min over a diffraction angle (2θ) range of 5° to 90°.

Hydrophilicity and Surface Roughness

The scaffold's hydrophilicity was assessed through the measurement of water contact angle with a contact angle goniometer (atPhysicics-oca20, Germany). Additionally, the surface roughness of the samples was analyzed using a laser confocal scanning microscope (OLS5000, Japan).

In vitro Cell Studies

Isolation and Culture of BMSCs

Bone marrow-derived mesenchymal stem cells (BMSCs) from rats were isolated using the whole bone marrow adherence method. Briefly, three-week-old male SD rats were euthanized, and under sterile conditions, bilateral femurs and tibias were harvested. The bone marrow cavities were exposed to collect BMSCs, which were then cultured in 10 mL of DMEM/F-12 medium (Gibco, C11330500BT) supplemented with 10% fetal bovine serum (FBS, Sigma, AUS) and 1% penicillin-streptomycin (Beyotime, C0222). The cells were incubated under standard culture conditions (37°C, 5% CO_2). The culture medium was replaced daily, and when cells reached 80% confluency, they were passaged. Third-generation BMSCs were seeded onto scaffolds at a density of 1×10^5 cells/mL.

LIPUS Stimulation

The low-frequency pulsed ultrasound therapy device (LIPU-ST IM330) was developed and provided by Shenzhen Shengxiang High-Tech Co., Ltd. In vitro experiments were conducted using the LIPUS device, which was set to a sine wave frequency of 1.0 MHz, a pulse repetition frequency of 1 kHz, an intensity of 30 mW/cm², and a duty cycle of 20%. An adequate amount of degassed water was placed in the ultrasound tank, and a 12-well plate containing the scaffolds for co-culturing with cells was positioned on the ultrasonic transducer (with an area of 4 cm²). Starting from the day of seeding, the bottom of the culture plates was stimulated for 10 minutes daily. To prevent energy from the LIPUS from indirectly transferring to adjacent wells, the scaffolds were distributed in every other well of the 12-well plate (with one empty well in between). The samples were divided into four groups: (1) pure polylactic acid (PLA); (2) polylactic acid/barium titanate (BT/PLA); (3) polylactic acid with low-intensity pulsed ultrasound (PLA + LIPUS); and (4) polylactic acid/barium titanate with low-intensity pulsed ultrasound (BT/PLA + LIPUS).

Cell Proliferation

The scaffolds were ultraviolet-irradiated for 1 hour and then rinsed 3 times with sterile PBS. Subsequently, the scaffolds were transferred to new 12-well plates, and DMEM/F12 complete medium was added; the scaffolds were then soaked for 24 hours for pre-wetting. The resulting third-passage cells were prepared into a cell suspension of appropriate concentration, with the seeding density adjusted to 1×10^5 cells/mL. The assessment of cell proliferation on the scaffolds was conducted at 1, 4, and 7 days following incubation through the utilization of the CCK-8 assay. At every specified time interval, the scaffolds were moved from their original plates to fresh 12-well plates, which were complemented with 2 mL of complete culture medium and 200 μL of CCK-8 reagent in each well. After incubating for 1 hour in a cell culture incubator, 100 μL of the liquid from each well was collected, and the absorbance was recorded at 450 nm utilizing a microplate reader.

Cell Adhesion and Morphology

BMSCs were seeded onto the scaffold at a density of 1×10^5cells/mL. After incubation for 6 hours, the scaffold was rinsed with PBS, and the number of detached cells was counted to calculate the cell adhesion rate on the various scaffolds. Furthermore, following a 4-day co-culture of the cells with the scaffold, the cellular morphology on the scaffold was examined utilizing scanning electron microscopy (SEM; Tescan, Amber, Czech Republic) as well as confocal laser scanning microscopy (CLSM; LSM980, Zeiss).

Cytotoxicity

The assessment of cytotoxicity for the scaffold was performed through the Live/Dead assay. At a concentration of 1×10^5 cells/mL, BMSCs were cultured on the scaffolds. After a 4-day incubation period under different conditions, the cells underwent staining with the Calcein-AM/PI Double Stain Kit (Calcein-AM/PI Live/Dead Cell Staining Kit, Yeasen) and were kept in the dark for 15 minutes. Cell viability was analyzed using a laser confocal scanning microscope (CLSM), where live cells exhibited green fluorescence and dead cells displayed red fluorescence.

ALP Activity and Calcium Nodule Deposition

BMSCs were seeded onto the scaffolds at a density of 1×10^5 cells/mL and cultured using the OriCell® Rat Bone Marrow Mesenchymal Stem Cell Osteogenic Induction Differentiation Kit (RAXMX - 90021, China). After 7 and 14

days of incubation, alkaline phosphatase (ALP) staining and alizarin red staining were performed. After staining, excess dye was gently rinsed off with distilled water, and the culture plates were observed under an inverted microscope to evaluate the osteogenic staining results.

Gene Expression Was Assessed by qRT-PCR

Cells co-cultured with the scaffolds for 7 days were collected, and total RNA was extracted using the Trizol reagent kit. After assessing the purity and concentration of the RNA, reverse transcription was performed to synthesize cDNA, followed by qRT-PCR amplification. Utilizing glyceraldehyde-3-phosphate dehydrogenase (GAPDH) as a reference gene, the average normalized expression ratio was calculated with the efficiency-corrected 2-ΔΔCt method. The gene expression was determined in comparison with the blank control group, and the corresponding primer sequences of the genes are listed in Table 1.

In vivo Studies

Animal Model and Scaffold Implantation

In this study, we utilized 36 male SD rats, each weighing around 250 g, which were sourced from the animal center of Harbin Medical University, to create a critical-sized cranial defect model with a diameter of 5 mm. The study protocol was approved by the Ethics Committee of Harbin Medical University (Approval No. YJSDW2023-175) and conducted in accordance with the Guide for the Care and Use of Laboratory Animals published by the National Institutes of Health (NIH). PLA and BT/PLA scaffolds were implanted at the defect site, while a control group without scaffolds served as the blank control. The animals were randomly divided into the following six groups: (1) Control; (2) PLA; (3) BT/PLA; (4) Control + LIPUS; (5) PLA + LIPUS; (6) BT/PLA + LIPUS. Post-surgery, animals in the ultrasound group were exposed to LIPUS, with device parameters consistent with those described in previous cellular studies. A handheld transducer was placed on the rats' heads, and a thin layer of coupling agent was applied to ensure proper contact. The treatment was administered for 20 minutes daily, and the animals were euthanized 8 weeks after implantation.

In vivo Biocompatibility Assessment

After eight weeks, liver and kidney tissues from the experimental animals were collected for analysis. The samples were preserved in 4% paraformaldehyde for a duration of 48 hours, subsequently embedded and sliced. To assess the biocompatibility of the scaffolds in a living organism, staining with hematoxylin and eosin (H&E) was conducted.

Micro-CT Analysis

The osteogenesis effect of the scaffolds was evaluated by Micro-CT (SkyScan 1276, Bruker, Germany) analysis. Positioned in the sample holder, the specimens underwent scanning with the following parameters: a scanning resolution near 9 μm, a rotation angle of 360°, a source voltage set to 85 kV, and a current of 200 μA. Parameter analysis was conducted using CT Analyser (CTan) v.1.18.8.0 (Bruker) to obtain two - dimensional images, while three-dimensional Micro-CT images were generated using Mimics Research 21.0.0.406 software (Materialise NV). The region of interest (ROI) for the implants was defined as D:5 mm, H:1 mm, with a threshold for new bone set between 115–255. Subsequently, three-dimensional reconstruction of the ROI images was performed to assess the three- dimensional

Table 1 Primers Used in Real-Time PCR

Gene	Forward Primer Sequence (5′-3′)	Reverse Primer Sequence (5′-3′)
ALP	CATGTTCCTGGGAGATGGTATG	GTGTTGTACGTCTTGGAGAGAG
Runx2	GCCACTTACCACAGAGCTATTA	GGCGGTCAGAGAACAAACTA
Col-I	ACTGGTACATCAGCCCAAAC	GGAACCTTCGCTTCCATACTC
OPN	AGGAGTTTCCCTGTTTCTGATG	GCAACTGGGATGACCTTGATA
PI3K	ACAGGCACAACGACAACATCA	TAAGCCCTAACGCAGACATCC
Akt	CTTCTACGGTGCGGAGATTGT	GTCCTTGTCCAGCATGAGGTT
GAPDH	ACTCCCATTCTTCCACCTTTG	CCCTGTTGCTGTAGCCATATT

structure of the cranial defect and regeneration. Finally, an analysis of the statistics was conducted regarding the bone volume fraction (BV/TV) and the bone mineral density (BMD) in the defined region of interest (ROI).

Histological Examination

The collected hard tissue specimens were stained to further investigate the bone integration of the implanted scaffolds. For histological analysis, all sections were treated with hematoxylin and eosin (H&E) as well as Masson's trichrome staining. Histological images were obtained using a standard optical microscope. The area covered by the newly generated bone tissue was assessed with ImageJ software, allowing for a qualitative evaluation of the newly formed bone 8 weeks post-implantation.

High-Throughput Sequencing

BMSCs were seeded in 12 - well plates at a density of 1×10^5 cells/mL and then co - cultured with scaffolds from the PLA + LIPUS and BT/PLA + LIPUS groups under the same conditions. After 7 days of co - culture, RNA was collected from each group for transcriptome sequencing.

The sequencing results were analyzed for differential gene expression using the limma R package, comparing the PLA + LIPUS group with the BT/PLA + LIPUS group. Genes were selected based on the criteria of $p \leq 0.05$ and $|\text{fold change (FC)}| \geq 1.5$. Subsequently, the differentially expressed genes were uploaded to the DAVID database (https://david.ncifcrf.gov/) for enrichment analysis, and the results were visualized for relevant KEGG pathways, biological processes (BP), cellular components (CC), and molecular functions (MF). Additionally, the differentially expressed genes were uploaded to the STRING database (https://cn.string-db.org/), selecting "Rattus Norvegicus" for protein-protein interaction (PPI) network analysis. The results were processed using Cytoscape_v3.10.1 software, and the CytoNCA plugin was applied to calculate the Degree values for each target, which were then ranked and visualized to display the related network.

Statistical Analysis

Analysis of the data was carried out using GraphPad Prism version 10.1.0. All experiments were executed in triplicate, and the results are displayed as the mean ± standard deviation (SD). Comparisons between different conditions at each time point were made using one-way ANOVA, followed by multiple comparisons with the least significant difference (LSD) method. A p-value below 0.05 was deemed statistically significant.

Results

Selection and Characterization of the Optimal Ratio for Composite Scaffolds

Shape Memory Property of the Scaffold

The deformation, shape retention, and recovery processes of BT/PLA composite materials with different percentages of BT are illustrated in Figure 1a. All five groups of the materials completed the shape recovery process within 5 seconds, exhibiting a high shape recovery rate of more than 96.5%, demonstrating excellent shape memory performance. Notably, the BT/PLA group containing 20 wt% BT exhibited the fastest recovery speed and the highest recovery rate among the five groups (Figure 1b). Additionally, the shape recovery tests indicated that the material softens rapidly at elevated temperatures (above Tg), allowing for versatile shaping and enhancing its adaptability. Furthermore, the material exhibits a relatively slow cooling rate at room temperature, resulting in a gradual transition from the elastomeric state to the glassy state. This extended timeframe facilitates precise and meticulous shaping, allowing clinicians to administer more accurate treatment to the patient's injured area.

SEM and EDS Analyses

With the aid of FDM technology, we successfully fabricated composite scaffolds with precise pore structures. The scaffolds exhibit a smooth surface, and both pore diameter and porosity are well-controlled, showing no significant deviation from the design model. The SEM images and EDS spectra of BT/PLA scaffold samples with varying BT content are shown in Figure 1c. Under high magnification, the BT/PLA scaffold surfaces reveal protruding BT particles, indicating that barium titanate is uniformly dispersed within the polylactic acid matrix at 15% and 20% BT content.

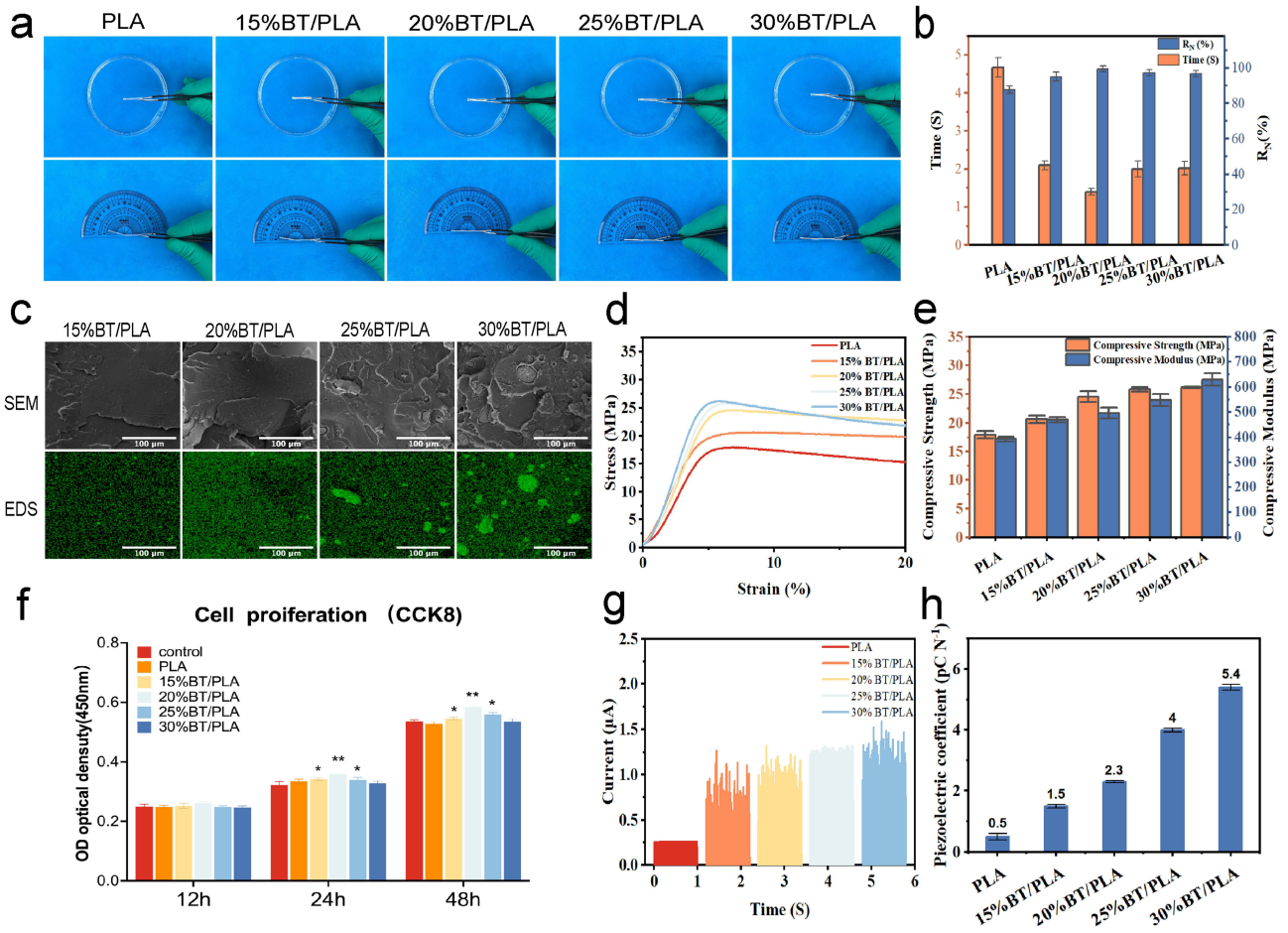

Figure 1 Assessment of Mechanical Properties, Shape-Memory Function, and Piezoelectric Performance of Various Scaffolds. (**a**) Shape-memory images of the scaffolds. (**b**) Recovery rate and recovery time of the scaffolds. (**c**) SEM and EDS analysis of scaffold cross-sections. (**d**) Stress-strain curves. (**e**) Bar graphs showing compressive strength and modulus (n=3). (**f**) Cell proliferation on different scaffolds (n=3). (**g**) Short-circuit current measurements of different scaffolds. (**h**) Piezoelectric constant (d33) of different scaffolds (n=3). Statistical significance is indicated by asterisks: *P < 0.05, **P < 0.01, ***P < 0.001.

However, at 25% and 30% BT content, a noticeable agglomeration of BT occurs within the composite material. This suggests that as the BT content increases, the nanoscale BT tends to agglomerate, hindering its effective dispersion in the PLA matrix and consequently impacting the shape memory properties of the material.

Compressive Strength and Elastic Modulus

Compressive strength, also known as ultimate strength, measures the ability of the scaffold to maintain structural integrity under external forces. The elastic modulus is the proportionality constant between stress and strain during the elastic deformation phase, reflecting the material's resistance to elastic deformation. Figure 1d and e present the histograms of the stress-strain curves, compressive strength, and elastic modulus of the scaffolds. The compressive strength of the PLA scaffold is 17.92 ± 0.65 MPa, while the compressive strengths of 15% BT/PLA, 20% BT/PLA, 25% BT/PLA, and 30% BT/PLA are 20.63 ± 0.63 MPa, 24.55 ± 0.96 MPa, 25.84 ± 0.37 MPa, and 26.19 ± 0.14 MPa, respectively. The elastic modulus of the PLA scaffold is 392.5 ± 9.46 MPa, and the elastic modulus of 15% BT/PLA, 20% BT/PLA, 25% BT/PLA, and 30% BT/PLA are 469.4 ± 11 MPa, 496.6 ± 22.3 MPa, 547.0 ± 23.8 MPa, and 629.5 ± 24.4 MPa, respectively. Notably, the compressive strength and modulus of all scaffolds in this study are within the normal range of human cancellous bone. (compressive strength: 0.2–80 MPa; modulus: 10–2000 MPa), meeting the basic requirements for bone repair.[33] Furthermore, as the mass fraction of BT nanoparticles increases, the compressive strength and modulus show an upward trend. This indicates that an increase in BT nanoparticles within a certain range can improve the mechanical characteristics of the composite scaffold.

Piezoelectric Property of BT/PLA Scaffold

As shown in the Figure 1g and h, Under low-frequency ultrasound, both the output current and piezoelectric constant of the BT/PLA scaffold increase with the increase in BT content. According to relevant literature, bioelectric currents in vivo range from 10^{-3} to 10 μA,[34] while the piezoelectric constants of bone tissue are reported to be 0.7–2.3 pC N^{-1}.[16] Our findings reveal that the piezoelectric constant of the 20% BT/PLA group is 2.3 pC N^{-1}, closely matching that of bone tissue, with the scaffold generating approximately 1 μA of current under low-frequency ultrasound. Therefore, theoretically, the 20% BT/PLA scaffold is well-suited for cell and bone tissue repair and holds promise for further experiments.

Biocompatibility of BT/PLA Scaffolds with Different BT Content

After co-culturing cells with composite scaffolds containing different BT concentrations for 12, 24, and 48 hours, cell proliferation in each group was assessed using the CCK-8 assay. We observed an increasing trend in OD values in all groups, indicating that the number of cells increased over time. As shown in Figure 1f, at 12 hours, the OD values in all groups were similar, with no statistically significant differences, although the OD value for the 20% BT/PLA group was slightly higher. However, at 24 and 48 hours, the OD values of cells on the 20% BT/PLA scaffold were significantly higher than those of the Control group ($p<0.01$), indicating that the 20% BT/PLA composite scaffold is more conducive to cell growth.

To sum up, the 20% BT/PLA scaffold displays excellent shape recovery rate, mechanical properties, piezoelectric performance, and biocompatibility, and is most suitable for bone regeneration. Therefore, the 20% BT/PLA scaffold was selected for subsequent experiments to verify its osteogenic potential both in vitro and in vivo.

The Microstructural Characterization of BT/PLA Composite Scaffolds

After selecting the optimal ratio for the composite scaffold, we further characterized the PLA and 20% BT/PLA scaffolds. We observed that the scaffold containing BT appeared milky white to the naked eye (Figure 2a1), while the PLA scaffold was transparent (Figure 2b1). SEM analysis revealed no significant changes in surface morphology of PLA and BT/PLA scaffolds at low magnification (Figure 2a2 and 22). However, at higher magnification, notable differences were observed (Figure 2a3 and 23). At a magnification of 2000x, the surface of BT/PLA exhibited numerous small wrinkles and particulate protrusions, while the surface of PLA remained smooth and even. EDS data (Figure 2c and d) confirm the successful fabrication of the composite scaffolds, as the presence of barium (Ba) was detected. The quantitative analysis of Ba content aligns with the experimental design (Figure 2d). Further observation of the morphology of BT (Figure 2e) and BT/PLA (Figure 2f) nanoparticles was conducted using TEM. The results show that high-temperature treatment did not alter the nanocrystalline structure of BT. The elemental distribution, as measured by EDS, is shown in Figure 2h–L, and the distribution of elements correlates well with the TEM images. The distribution of C and Ba elements indicates that BT nanoparticles are well dispersed within the PLA matrix. These results further confirm the successful fabrication of the BT/PLA composite scaffolds.

XRD Analysis

As shown in Figure 2g, we observed that PLA exhibits characteristic peaks of the typical α-crystalline form, located at approximately 16.5°, 18.9°, 22.3°, and 26.7°. The same characteristic peaks appeared in the composites after the addition of BT. All the additional diffraction peaks correspond to the BT particles themselves, indicating that the crystalline structure of PLA remains unchanged and continues to exist in the α-crystalline form within the composite system. Therefore, it is highly likely that the composite retains PLA's properties of biocompatibility, biodegradability, and shape memory characteristics.

Hydrophilicity and Surface Roughness

As shown in Figure 3a1, 2, and c, we observed that the water contact angle of the BT/PLA scaffold is smaller than that of the PLA scaffold ($p<0.05$), indicating that the BT/PLA scaffold shows better hydrophilicity than PLA. In other words, the incorporation of BT particles successfully enhanced the hydrophilicity of PLA. Therefore, compared with the PLA scaffold, the BT/PLA scaffold is more conducive to cell adhesion. Additionally, the inclusion of BT particles significantly increased the surface roughness of the scaffold (Figure 3b1, 2 and d) ($p<0.05$). These results suggest that the BT/PLA scaffold has a larger specific surface area than PLA, which is beneficial for cell attachment and adhesion.

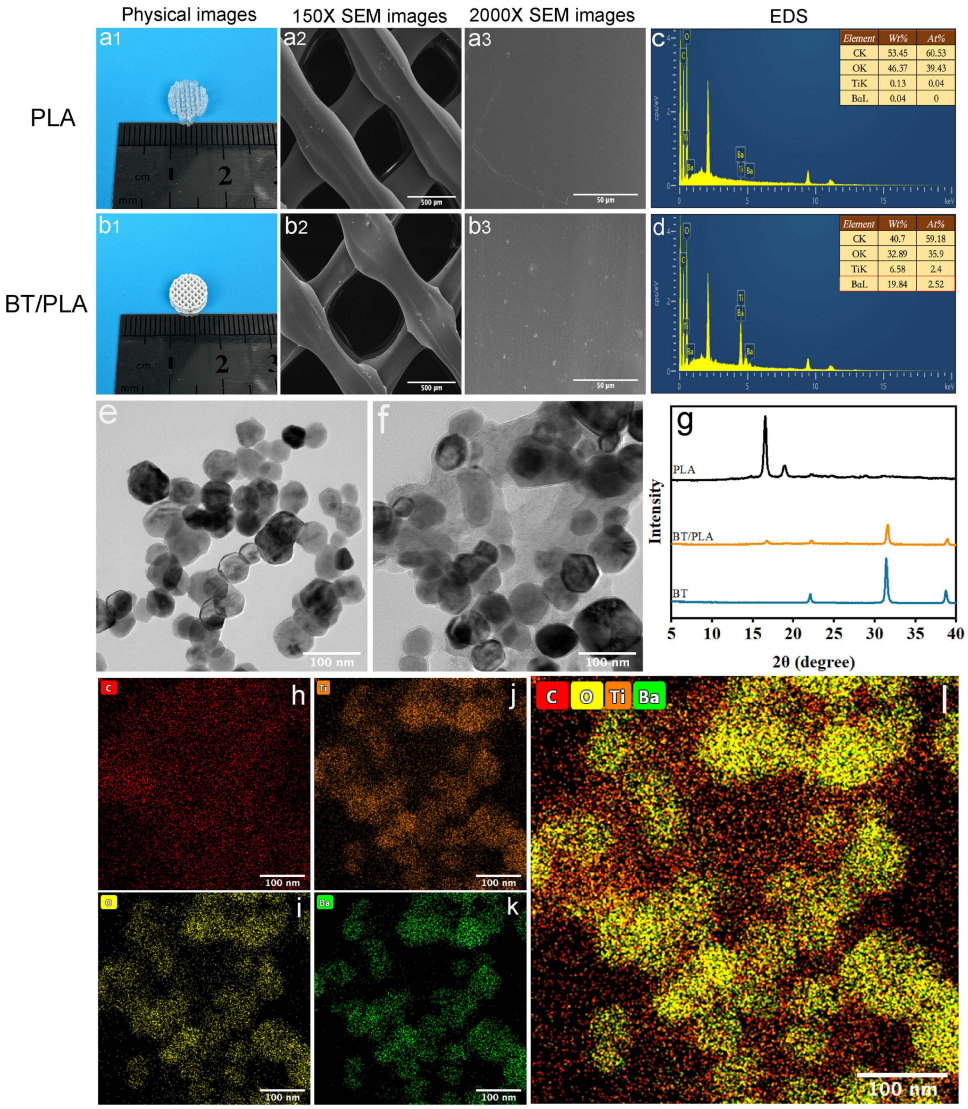

Figure 2 SEM and TEM Imaging for Structural and Morphological Characterization of the scaffold. (**a1**–**a3**) Macroscopic views and SEM images of surface morphology of PLA scaffoldand (**b1**–**b3**) BT/PLA scaffold. (**c**) EDS data of PLA scaffold and (**d**) BT/PLA scaffold. (**e**) The TEM images of BT and (**f**) BT/PLA scaffold. (**g**) XRD patterns of the scaffolds. (**l**) Energy dispersive spectrometer element mapping of BT/PLA nanoparticles and corresponding element mappings: (**h**) C, (**i**) O, (**j**) Ti, (**k**) Ba.

In vitro Testing

Proliferation of Cells

Cell proliferation in each group was evaluated after 1, 4, and 7 days of co-culturing with the scaffolds using the CCK-8 assay. Across all groups, cell viability showed a clear increase as the incubation period was extended (Figure 4d). On day 1, however, the cell viability in the ultrasound-treated groups was marginally lower compared to the control groups, which may be attributed to the effect of LIPUS on cell attachment. By day 4, cell viability was significantly greater in the BT/PLA, PLA+LIPUS, and BT/PLA+LIPUS groups compared to the PLA group ($p<0.05$). Moreover, the cell viability in the BT/PLA+LIPUS group surpassed that of both the BT/PLA and PLA+LIPUS groups ($p<0.05$), with no notable difference between the BT/PLA and PLA+LIPUS groups. After 7 days of incubation, the trends remained consistent with those observed on day 4. These data suggest that the addition of BT does not exhibit cytotoxicity but rather promotes cell proliferation to some extent. Moreover, under LIPUS stimulation, the piezoelectric effect of the BT/PLA composite material is activated, further promoting cell proliferation, with the combination of both leading to higher cell survival rates.

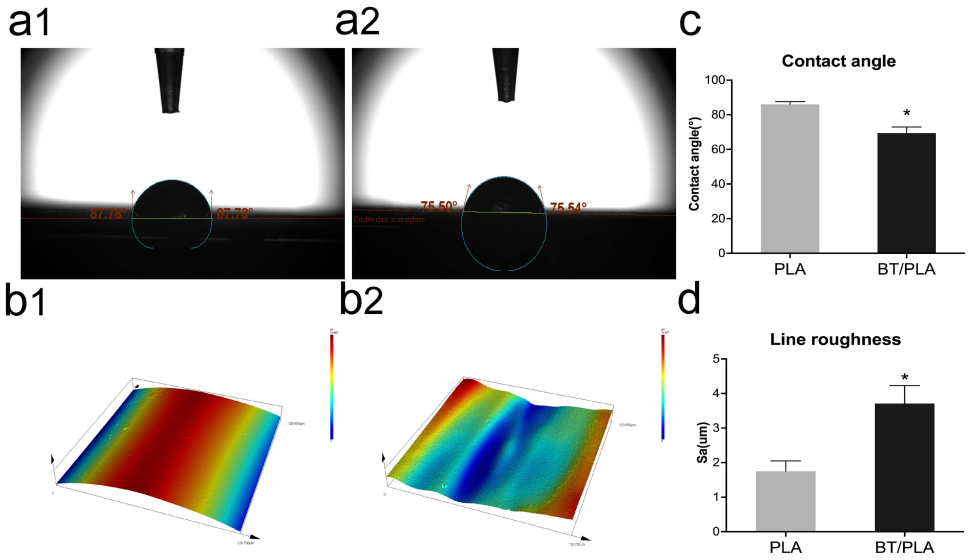

Figure 3 Water Contact Angle Measurement and Surface Characterization of PLA and BT/PLA Scaffolds. (**a1**) Water contact angle measurement of the PLA scaffold and (**a2**) BT/PLA scaffold. (**c**) Analysis of average water contact angles (n=3). (**b1**) Surface CLSM images of the PLA scaffold and (**b2**) BT/PLA scaffold. (**d**) Surface roughness analysis (n=3). Asterisks (*) indicate statistical significance, *P< 0.05.

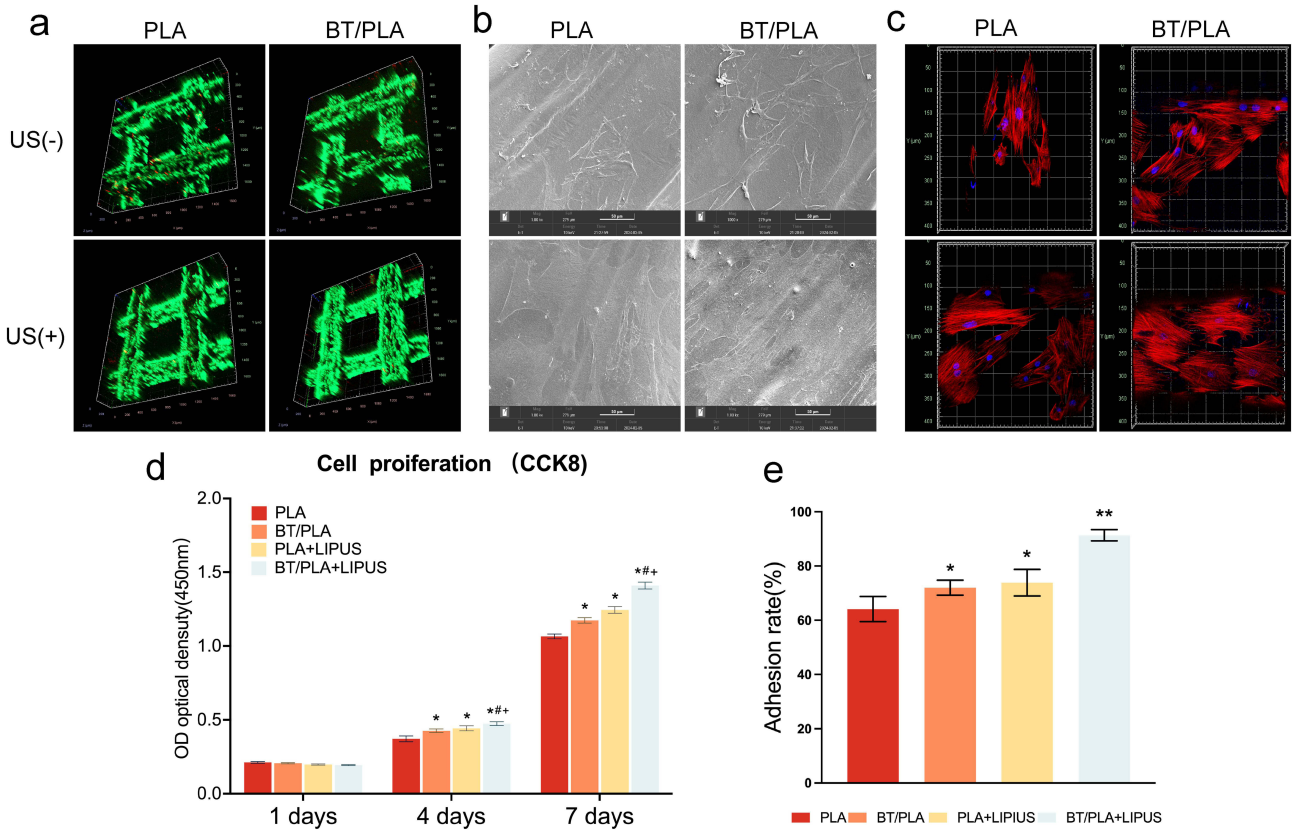

Figure 4 Images of BMSCs Co-cultured with Scaffolds for 4 Days. (**a**) Live/dead cell staining. (**b**) SEM images. (**c**) Fluorescent staining of cells (red: rhodamine-phalloidin for F-actin; blue: DAPI for nuclei). (**d**) CCK-8 assay of cell proliferation in each group (n=3), (*p < 0.05 vs PLA, #p < 0.05 vs BT/PLA, +p < 0.05 vs LIPUS+PLA). (**e**) Cell adhesion rate on different scaffolds (n=3), (Asterisks (*) denote statistical significance when compared to the PLA group: *P < 0.05, **P < 0.01, ***P < 0.001). (US+ and US− indicate the presence or absence of ultrasound treatment during culture, respectively).

https://doi.org/10.2147/IJN.S524080

Cytotoxicity of the Scaffolds

After co - culturing with the scaffolds for 4 days, a live/dead assay was performed to analyze the cytotoxicity of the scaffolds. Figure 4a illustrates that live cells are represented by green fluorescence, whereas dead cells are indicated by red fluorescence. The results showed that cells grew well on all scaffolds. Only a small number of dead cells were observed on the PLA scaffolds, while no obvious cell death was detected on the other scaffolds, indicating that all groups of scaffolds possess good cytocompatibility. Notably, the green fluorescence intensity in the BT/PLA group, the PLA + LIPUS group, and the BT/PLA + LIPUS group was higher than that in the PLA group. Furthermore, the green fluorescence intensity in the BT/PLA + LIPUS group exceeded that of both the BT/PLA and PLA + LIPUS groups, with minimal differences observed between the BT/PLA and PLA + LIPUS groups. This suggests that LIPUS activates the piezoelectric effect of the material, thereby enhancing cell activity and resulting in increased cell viability.

Cell Adhesion and Morphology

On day 4, the BMSCs were stained with fluorescent markers to examine their adhesion and the morphology of the cytoskeleton. F-actin was labeled with Actin-Tracker Red-594 and nuclei were labeled by DAPI (Figure 4c). Based on CLSM observations, we found that cells in the BT/PLA + LIPUS group were well spread across the scaffold and had superior morphology compared to the other three groups. The cells displayed a polygonal spreading pattern, supported by organized F-actin, with no evident nuclear abnormalities. In addition, by calculating the cell adhesion rate on different scaffolds (Figure 3e), we observed that cells in the BT/PLA + LIPUS group had the highest cell adhesion ratio. The findings suggest that after LIPUS stimulation, the scaffold's piezoelectric effect enhances cell adhesion and promotes growth.

Figure 4b displays the SEM images of BMSCs that were co-cultured for four days under various conditions. In the PLA group, the BMSCs exhibited stretched pseudopodia, yet they were distributed sparsely and seemed to be atrophied on the scaffold. In contrast, the BT/PLA, PLA + LIPUS, and BT/PLA + LIPUS groups had healthier appearances and higher cell densities. Specifically, BMSCs adhering to the surface of the BT/PLA + LIPUS scaffold grew normally, exhibiting spindle or polygonal shapes with a more natural morphology and better adhesion than those in the other three groups. This improvement in cell adhesion can be attributed to the increased surface roughness of the material due to the incorporation of BT nanoparticles into the PLA, which facilitates cell attachment. More importantly, the composite material demonstrated its inherent piezoelectric effect under LIPUS stimulation, which enhanced cell vitality and adhesion strength in response to electrical signals. These results indicate that both BT and LIPUS promote better cell adhesion and growth, and their combination has an even greater effect.

In vitro Osteogenic Differentation

The determination of osteogenic differentiation in BMSCs was assessed through ALP activity, calcium nodule formation, and the expression of genes related to osteogenesis.

The ALP staining results after co-culturing BMSCs with PLA and BT/PLA scaffolds for 7 days are shown in Figure 5a and c. The control group showed no difference in the ALP-positive area between cells cultured with and without ultrasound stimulation, indicating that ultrasound does not affect cell differentiation. The ALP activity was elevated in the BT/PLA + LIPUS, PLA + LIPUS, BT/PLA, and PLA groups compared to the control group. Notably, the ALP activity in the BT/PLA + LIPUS group was significantly higher than that in the PLA, BT/PLA, and PLA + LIPUS groups. Additionally, the ALP activity in the BT/PLA + LIPUS group was 1.6-fold higher than that in the Control group. However, no significant difference was observed between the PLA + LIPUS and BT/PLA groups. These findings indicate that the surface charge of the scaffolds may play a role in influencing the differentiation of BMSCs.

After co-culturing for 14 days under different conditions, the osteogenic activity was further validated through Alizarin Red staining (Figure 5b and d). Notably, the ultrasound-treated BT/PLA scaffold exhibited a significantly higher number of mineralized nodules compared to the Control group and PLA scaffold, with its mineralization capacity being 3.9-fold that of the Control group. This indicates a marked enhancement in osteogenic differentiation of the ultrasound-treated BT/PLA scaffold. The Alizarin Red staining results are consistent with the ALP staining findings, indicating that the BT/PLA scaffold under LIPUS effectively promotes osteogenic differentiation.

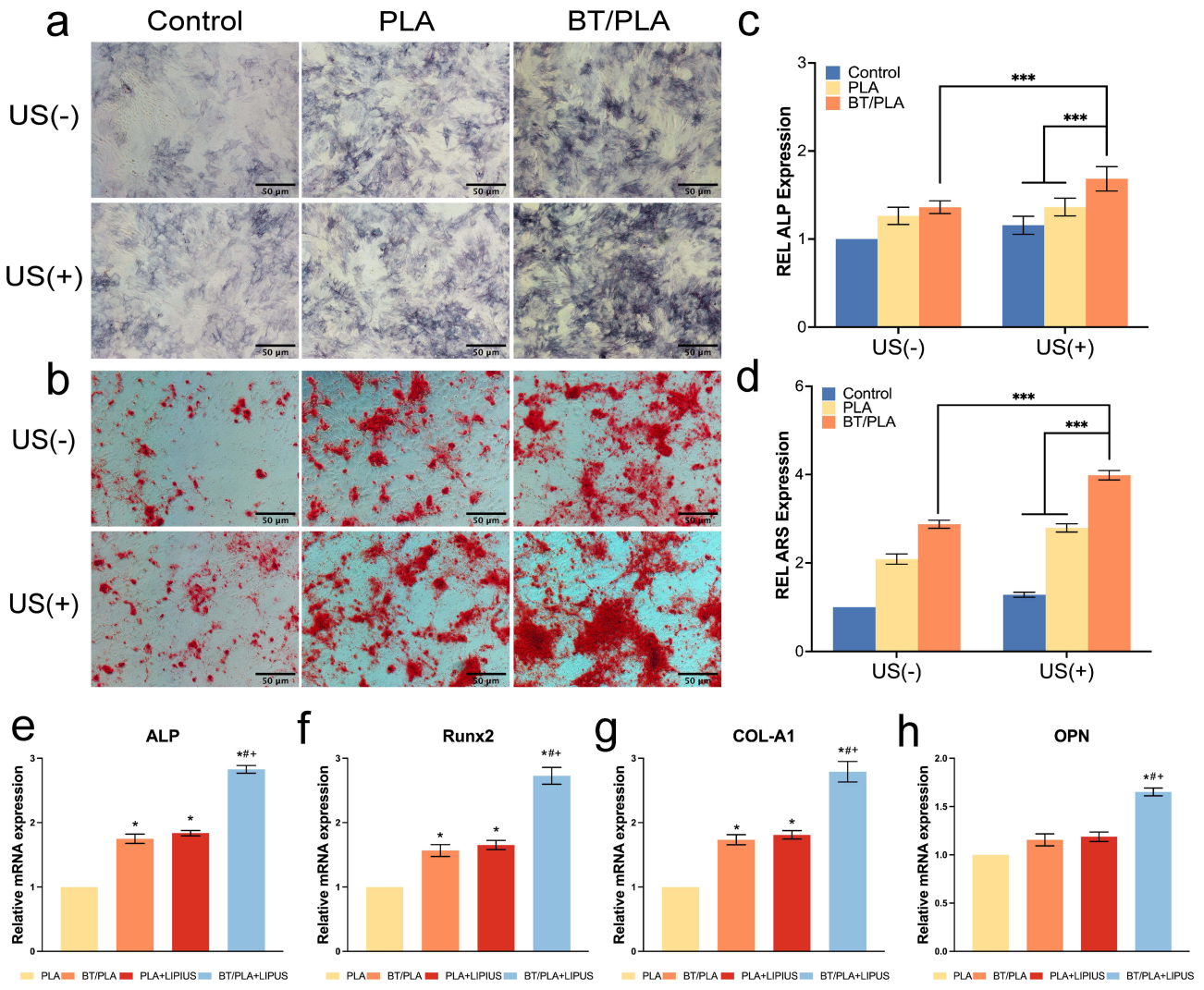

Figure 5 Osteogenic Differentiation of BMSCs on Scaffolds. (**a**) ALP staining images of BMSCs co-cultured with scaffolds for 7 days. (**b**) ARS staining images of BMSCs co-cultured with scaffolds for 14 days. (**c** and **d**) Statistical analysis of ALP and ARS staining images (n=3), (US+ and US− indicate the presence or absence of ultrasound treatment during culture, respectively; asterisks (*) denote statistical significance, *P < 0.05, **P < 0.01, ***P < 0.001). Relative mRNA expression of ALP (**e**), Runx2 (**f**), COL-A1 (**g**), and OPN (**h**), *p < 0.05 vs PLA, $^{\#}$p < 0.05 vs BT/PLA, and +p < 0.05 vs PLA+LIPUS.

The expression levels of ALP, Runx2, Col-1, and OPN were evaluated using RT-PCR. Figure 5e–g, and h illustrates that the mRNA levels of ALP, Runx2, Col-1, and OPN were markedly elevated in the BT/PLA + LIPUS group compared to the other three groups, with ALP showing a 2.8-fold increase ($p<0.05$), Runx2 a 2.7-fold elevation ($p<0.05$), Col-1 a 2.7-fold upregulation ($p<0.05$), and OPN a 1.6-fold rise ($p<0.05$). No significant differences were observed between the PLA + LIPUS and BT/PLA groups, both of which exhibited significantly higher expression levels compared to the PLA group.

In vivo Testing

Biocompatibility of the Scaffold in vivo

The biocompatibility of the scaffold was further evaluated through in vivo study. In Figure 6c, the liver and kidney tissue staining using H&E from various groups of rats is displayed. H&E staining clearly presented the morphological characteristics and cellular structure of the organs, and no significant damage or inflammation was observed, indicating that the 4D - printed 20%BT/PLA scaffold has good biocompatibility in vivo.

Bone Formation in vivo

Radiographic and histological assessments were conducted to examine the in vivo osteogenic potential of the scaffolds.

https://doi.org/10.2147/IJN.S524080

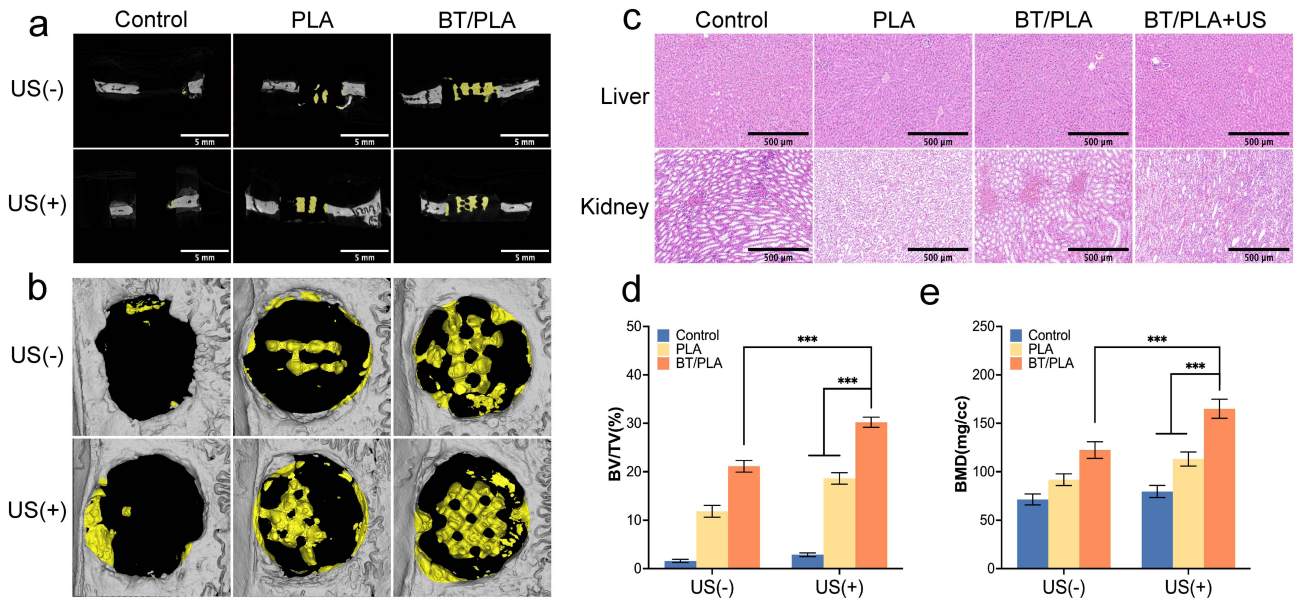

Figure 6 In Vivo Regeneration of Rat Cranial Defects. (**a**) Sagittal view and (**b**) top view of micro-CT images of cranial defect sites after 8 weeks. (**c**) H&E staining of liver and kidney after scaffold implantation under the rat's skin for 8 weeks. (**d**) Quantitative analysis of bone regeneration parameters (BV/TV). (**e**) Quantitative analysis of bone mineral density (BMD). (US+ and US− indicate the presence or absence of ultrasound treatment during culture; Asterisks (*) indicate statistical significance, *P < 0.05, **P < 0.01, ***P < 0.0001).

The three-dimensional Micro-CT reconstruction images (Figure 6a and b) revealed that, after 8 weeks, the healing of the bone defect in the blank control group was minimal, with only a small amount of new bone formation observed at the edges of the defect. In comparison, the BT/PLA + LIPUS group exhibited superior bone formation relative to the other groups, with new bone almost completely covering the entire bone defect. Furthermore, the extent of bone formation was quantitatively assessed using the bone volume to total volume (BV/TV) ratio. As shown in Figure 6d, the BV/TV values in the BT/PLA + LIPUS, PLA + LIPUS, and BT/PLA groups were markedly elevated compared to those in the PLA group. Additionally, the BV/TV in the BT/PLA + LIPUS group exceeded that of both the PLA + LIPUS and BT/PLA groups significantly; nonetheless, the differences observed between the PLA + LIPUS and BT/PLA groups were not statistically significant. In vivo Micro-CT analysis revealed that the bone volume to total volume ratio (BV/TV) of the 20% BT/PLA group was 28% higher than that of the Control group, which is consistent with in vitro observations showing that this scaffold promotes osteoblast differentiation. This synergistic effect indicates that the piezoelectric signals generated under low-intensity pulsed ultrasound (LIPUS) not only enhance cell proliferation in vitro but also accelerate bone remodeling in vivo. We also performed a quantitative analysis of bone mineral density (BMD) (Figure 6e). The experimental results indicated that, after ultrasound treatment, both PLA and BT/PLA scaffolds exhibited an increase in BMD, with the BT/PLA + LIPUS group showing a particularly significant enhancement. Compared to the Control + LIPUS and PLA + LIPUS groups, the BMD in the BT/PLA + LIPUS group was markedly higher. These results suggest that the BT/PLA scaffolds, under the influence of LIPUS, effectively promote bone formation and mineralization.

For H&E staining, none of the groups exhibited inflammation or pathological abnormalities (Figure 7a). In the control group, the defects exhibited minimal repair, with the majority of the area being filled by fibrous tissue. In contrast, the PLA, PLA + LIPUS, and BT/PLA groups showed the formation of bone bridges, but these were fragile, and noticeable gaps remained between the bone ends. In contrast, the BT/PLA + LIPUS group demonstrated a markedly higher osteogenic capacity. The bone bridge was uninterrupted and almost connected the two edges of the defect. It was challenging to differentiate the boundaries between the newly formed tissue and the native tissue. Nearly all of the scaffold's base was encased in newly formed bone, with noticeable bone growth also occurring inside the scaffold.

The results obtained from Masson's trichrome staining were similar to those from H&E staining (Figure 7b). In both the control and PLA groups, the defects stayed unhealed, with merely small and separate bone bridges having developed.

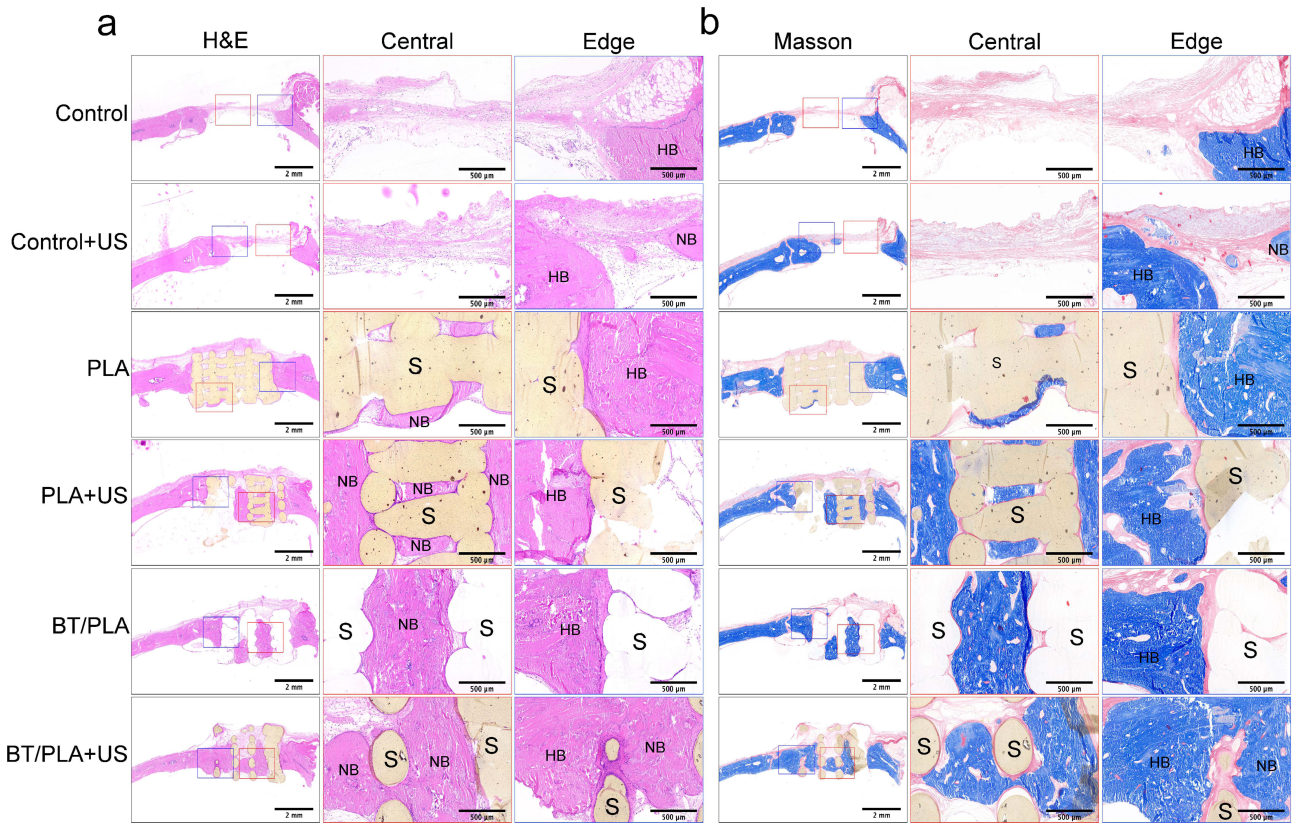

Figure 7 In Vivo Regeneration of Rat Cranial Defects. (**a**) H&E staining and (**b**) Masson's trichrome staining images of scaffolds embedded in tissue after 8 weeks of implantation. High-magnification images of scaffolds at the edge and central area of the defects.
Abbreviations: S, Scaffold; NB, new bone; HB, host bone.

Improved conditions were noticed in the PLA + LIPUS and BT/PLA groups, which exhibited partial healing. The BT/PLA + LIPUS group demonstrated superior bone formation, and the defects were nearly completely filled with woven bone (stained blue) and cortical - like lamellar bone (stained red). These histological staining results are in line with the Micro - CT scanning findings, suggesting that the combination of LIPUS and the piezoelectric effect of the scaffold significantly promotes bone regeneration.

The Piezoelectric Effect Activates the PI3K-Akt Pathway to Promote BMSC Proliferation and Osteogenic Differentiation

Screening of Differentially Expressed Genes

Based on the differential gene selection criteria, a total of 326 differentially expressed genes were identified in the BT/PLA + LIPUS group compared with the BT/PLA group, including 200 upregulated genes and 126 downregulated genes. Volcano plots and heatmaps were generated using the R language package (Figure 7a and b).

Differential Gene Enrichment Analysis

According to the analysis results from the David database, the KEGG enrichment pathways identified include the PI3K-Akt signaling pathway, and the enriched biological processes include cell differentiation. These findings may be related to the ability of the composite material to promote osteogenic differentiation in vitro and in vivo under low-frequency ultrasound (Figure 7e and f). Subsequently, based on the results from the String database, a total of 131 protein targets were enriched. Independent and unconnected targets were excluded from visualization. As shown in Figure 7c, there are 111 targets in total, with 52 interaction links representing the relationships between them. Then, the Degree values for each target were calculated using the CytoNCA plugin, and these values were visualized in ascending order.

https://doi.org/10.2147/IJN.S524080

Analysis of mRNA Expression of PI3K-Akt Pathway-Related Genes by RT-qPCR

Analysis of pathway enrichment through high-throughput sequencing indicated that the genes with differential expression in the BT/PLA and BT/PLA + LIPUS groups were linked to the PI3K-Akt signaling pathway. Accumulating evidence has established that the PI3K/AKT pathway is critically involved in diverse signal transduction cascades, including those governing cell proliferation, apoptosis, and differentiation, and serves as a pivotal regulator of bone regeneration across multiple biological systems.[35,36] To elucidate the mechanism by which the piezoelectric effect promotes osteogenic differentiation of BMSCs, we first examined the expression of PI3K and Akt genes in the BMSCs of the BT/PLA and BT/PLA + LIPUS groups. The findings indicated that in the BT/PLA + LIPUS group, the expression levels of the genes PI3K and Akt were significantly increased when compared to the BT/PLA group ($P<0.05$) (Figure 8d). To further verify whether the piezoelectric effect regulates osteogenic differentiation of BMSCs through the PI3K-Akt signaling pathway, we administered the PI3K-Akt pathway inhibitor, LY294002, to the BT/PLA + LIPUS group. The results demonstrated that LY294002 significantly downregulated the expression of PI3K and Akt compared to the BT/PLA + LIPUS group. Collectively, these experimental results suggest that the piezoelectric effect may promote osteogenic differentiation of BMSCs by activating the PI3K-Akt signaling pathway.

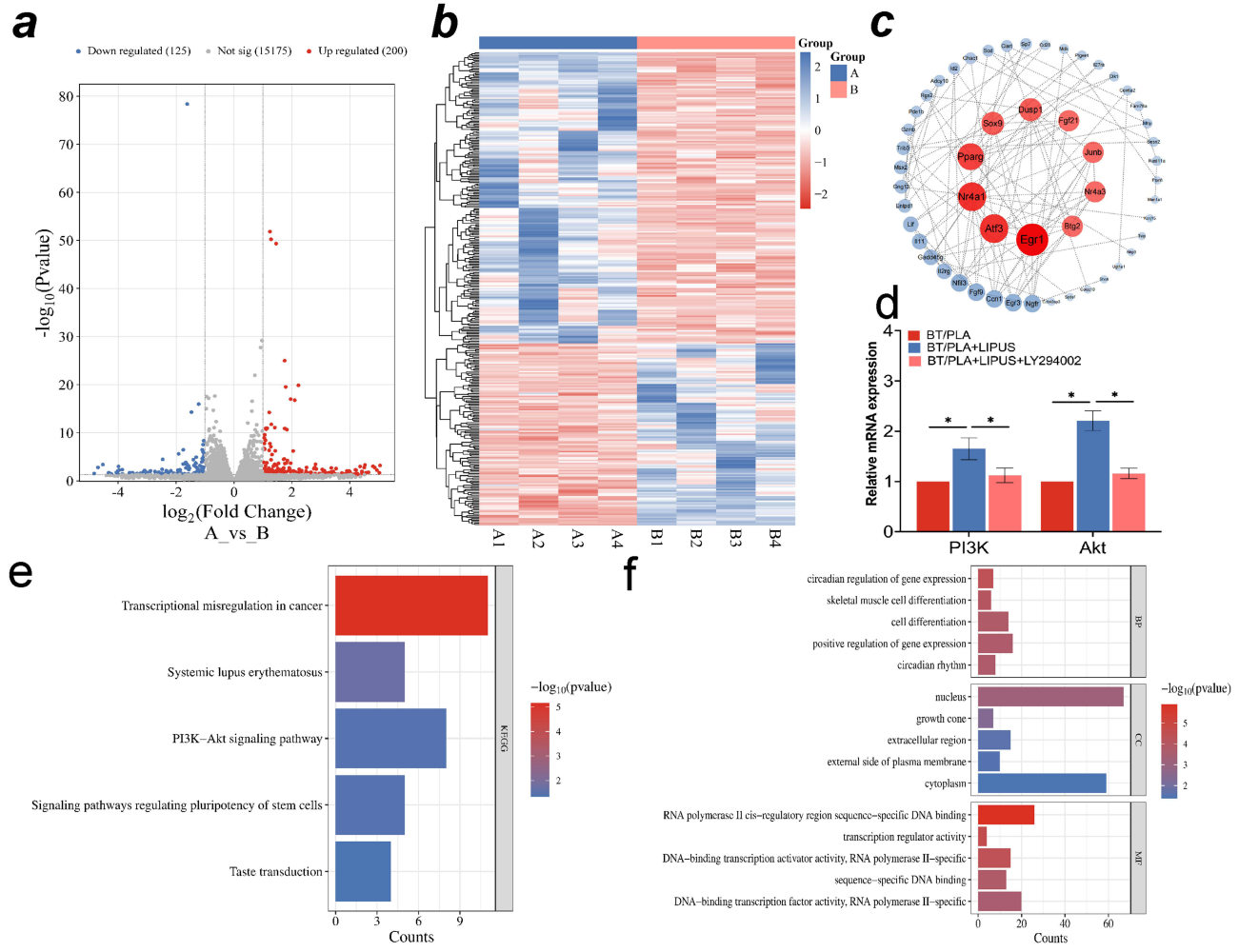

Figure 8 Differential Gene Analysis and Protein Interaction Network. (**a**) Volcano plot of differential genes. (**b**) Gene clustering heatmap. (**c**) PPI (protein-protein interaction) network diagram, where each circle represents a target gene, and the lines between circles indicate their interactions. The size of the circles reflects the importance of the targets, with larger circles representing greater significance. (**d**) Relative mRNA expression levels of PI3K and Akt before and after the addition of LY294002 in the BT/PLA+LIPUS group compared to the BT/PLA group (Asterisks (*) indicate statistical significance, *P< 0.05). (**e** and **f**) Results from KEGG, BP, CC, and MF analyses, where the x-axis represents the number of enriched entries, the y-axis represents the enriched terms, and the color indicates the P-value. (When more than five enriched terms are identified, only the top five terms with the lowest P-values are shown).

Discussion

Bone has the piezoelectric property of converting mechanical signals into electrical signals. When there is a bone defect, the local bioelectrical microenvironment changes, affecting bone repair and remodeling.[11–14] Presently, the bionic design of bone repair materials is mainly limited to the bionic imitation of composition, activity and structure, and there is insufficient attention to the role of bioelectrical effects in bone growth. The bionic reconstruction of the local electrical microenvironment through piezoelectric materials can provide an effective strategy for bone repair. In addition, the implantation of bone repair materials usually requires open surgery methods, which undoubtedly aggravates the destruction of the bone regeneration microenvironment. How to implant bone repair materials in a minimally invasive way is also a problem that needs to be solved clinically. Recently, shape memory intelligent polymers (SMPs) have drawn attention due to their advantages of good biocompatibility, processability and shape memory properties. Therefore, in this study, we construct a bionic electroactive BT/PLA composite scaffold with the dual advantages of shape memory and piezoelectricity. It can simultaneously meet the needs of minimally invasive implantation and reconstructing the local electrical microenvironment for bone regeneration.

For barium titanate (BT) piezoelectric ceramics, numerous studies have employed spraying techniques to fabricate BT coatings on metal surfaces. These methods yield dense-structured BT coatings with favorable mechanical properties, but issues such as uneven coating deposition and crack formation remain prevalent.[23,37] Therefore, in this study, we utilized 4D printing technology to prepare porous BT/PLA composite scaffolds. 4D printing, an extension of 3D printing with an added temporal dimension, enables printed objects to self-adjust their morphology in response to external environmental stimuli. Compared with conventional fabrication methods, this approach not only allows precise control over scaffold porosity and architecture but, more importantly, leverages its shape memory property to enable minimally invasive implantation of bone repair materials in clinical settings.[38]

Secondly, polylactic acid (PLA) was chosen as the carrier material due to its biodegradable characteristics as a degradable polymer, which has been widely applied in textiles, packaging, and biomedical fields. In vivo, PLA is hydrolyzed by hydrolases, converting the polymer into monomers that are metabolized into water and carbon dioxide.[39] Compared with polycaprolactone (PCL) and poly-L-lactic acid (PLLA), PLA exhibits a moderate biodegradation rate, which better matches the tissue healing process and reduces the risk of immune reactions.[27]

Characterization of the composites via TEM and XRD revealed that high-temperature treatment did not alter the nanocrystalline structure of BT, and BT was well-dispersed in the PLA matrix, confirming the successful fabrication of BT/PLA composite scaffolds. Shape recovery capability tests showed that all composite scaffolds with different BT loadings completed shape recovery within 5 seconds, demonstrating excellent shape memory properties. Compared to pure PLA scaffolds, BT-containing composites significantly enhanced recovery speed and ratio, with the 20% BT/PLA group exhibiting the fastest recovery kinetics and highest recovery rate. This superior performance is primarily attributed to the increased BT particle content, which notably improves the heating rate and enables more uniform heat distribution, thus effectively shortening the shape recovery time. Additionally, the material exhibits a slow cooling rate at room temperature, ie, a gradual transition from the rubbery to glassy state, which provides sufficient time for shape setting. However, when BT content exceeds a critical threshold, its impact on the material microstructure becomes evident. High BT loading strengthens intermolecular interactions in PLA, thereby restricting the mobility of polymer chain segments. This not only impairs the material's crystalline structure but also induces the gradual formation of particle aggregates within the composite, which negatively affects the scaffold's shape recovery performance. Mechanical property tests further showed that both compressive strength and modulus of the scaffolds trended upward with increasing BT nanoparticle mass fraction, indicating that within a specific range, BT fillers can reinforce the mechanical properties of the composite.

For piezoelectric materials, an external force is required to induce the generation of active electrons. However, long-term application of auxiliary external forces is impractical and inconvenient for patients. Studies have shown that barium titanate coatings fabricated on Ti6Al4V, when combined with LIPUS, can activate the piezoelectric effect of the scaffold, generating sufficient electrical current to upregulate the expression of osteogenesis-related genes and promote osteogenesis.[17] Other researchers have demonstrated that LIPUS can trigger the piezoelectric effect of piezoelectric

ceramics, thereby enhancing the activity of MC3T3-E1 cells.[40] Thus, we combined the BT/PLA composite scaffold with LIPUS to evaluate its piezoelectric performance.

Under low-intensity pulsed ultrasound (LIPUS) loading, the output current of the composite scaffolds showed consistency with piezoelectric constant measurements. As BT content increased, both the output current and piezoelectric constant of the scaffolds exhibited a significant upward trend. Piezoelectric constant measurements validated the differences in piezoelectric performance among scaffolds with varying BT contents, and all scaffold groups demonstrated favorable piezoelectric properties. Notably, the 20% BT/PLA group achieved a piezoelectric constant of 2.3 pC/N, which closely approximates the piezoelectric constant of bone tissue (d33 = 0.7–2.3 pC/N), indicating its remarkable advantages in biomimetic performance.[16]

Through comprehensive evaluations of shape recovery capability, mechanical properties, piezoelectric performance, and biocompatibility for composite piezoelectric scaffolds with varying BT contents, the 20% BT/PLA group was found to exhibit high shape recovery capacity while maintaining compressive strength and modulus within the normal range of human cancellous bone. Notably, its piezoelectric constant closely matched that of human bone tissue. Integrating these findings, we selected the 20% BT/PLA composite scaffold as the subject for further experiments to explore its bone repair capacity under LIPUS loading.

Biocompatibility of the scaffolds was systematically evaluated via cell viability, proliferation, adhesion, and morphology. Cell adhesion represents the initial step of cell-material interaction, as robust cell attachment to the scaffold is prerequisite for subsequent biological responses. The BT/PLA scaffold exhibited a significantly higher cell adhesion rate than the PLA scaffold, which can be attributed to the BT incorporation that effectively improved the surface microstructure properties of the PLA scaffold, manifested as remarkable enhancements in surface roughness and hydrophilicity. As documented in the literature, increased surface roughness of materials significantly improves cell adhesion capacity. Higher roughness not only provides more attachment sites for cells but also promotes biological interactions between cells and the scaffold, which are crucial for cell proliferation and differentiation.[41,42] Additionally, the hydrophilicity of the scaffold is closely associated with cell adhesion characteristics. In this study, BT/PLA scaffolds exhibited higher surface roughness and smaller water contact angles than PLA scaffolds. These improvements in surface properties create more favorable attachment conditions for cells, thereby promoting initial cell adhesion. This may facilitate the early-stage absorption of more serum proteins, inducing cells to secrete increased fibronectin and further promoting adhesion.[43]

The significant advantage of low-intensity pulsed ultrasound (LIPUS) in promoting cell survival was further confirmed by evaluating cell proliferation and viability across scaffold groups. Notably, under identical ultrasound stimulation, cells on BT/PLA scaffolds exhibited significantly higher viability than those on PLA scaffolds, indicating that the piezoelectric effect played a crucial role in enhancing cell activity. Cell viability serves as an intuitive indicator of growth status: live/dead cell fluorescence imaging showed that while all groups exhibited good cell viability, ultrasound-stimulated cells displayed notably higher activity, with the BT/PLA + LIPUS group demonstrating the highest fluorescence intensity. This suggests that the piezoelectric effect promotes cell activity, a finding also confirmed by Cai et al.[40]

To further explore the impact of scaffolds on BMSCs, we analyzed cell morphological characteristics via cytoskeletal staining. Results showed that BMSCs on PLA scaffolds predominantly exhibited contractile or fusiform shapes, whereas on BT/PLA and BT/PLA+LIPUS scaffolds, cytoskeletal structures were clearly visible, and cells displayed remarkable elongation. This morphological change is likely closely associated with the enhanced cell adhesion capacity of BT/PLA scaffolds, while combined LIPUS application further optimized cytoskeletal remodeling—similar findings were also observed in SEM images. In summary, these findings demonstrate that cell adhesion is influenced not only by BT nanoparticles but also by the electrical signals on the scaffold surface. LIPUS can activate the piezoelectric effect of the material, thereby promoting cell adhesion. Li et al demonstrated that BT not only promotes cell proliferation but also enhances the bioactivity of composite materials.[44] Ciofani et al synthesized water-soluble BT nanoparticles and reported that they exhibit both excellent biocompatibility and retain high dielectric constants and piezoelectric properties.[45] These findings are consistent with the results of this study.

Histological analyses of the liver and kidneys further validated the biocompatibility of all scaffold groups: none of the scaffolds induced inflammation, necrosis, or organ damage, confirming the absence of significant hepatotoxicity or

nephrotoxicity during in vivo use. These results not only highlight the biocompatibility advantages of BT/PLA scaffolds but also provide strong safety evidence for their potential applications in bone tissue engineering.

Osteogenic differentiation of cells was preliminarily evaluated via alkaline phosphatase (ALP) activity. Compared with BT/PLA and PLA+LIPUS groups, the BT/PLA+LIPUS group showed significantly higher ALP-positive areas and ALP activity, indicating that the piezoelectric effect of the scaffold might play a key role in enhancing ALP activity. Ultrasound stimulation increases the surface charge of BT/PLA scaffolds, further promoting cell proliferation and adhesion. This piezoelectric effect likely enhances intercellular signal transduction, creating a favorable microenvironment for cell adhesion and proliferation, thus laying an important foundation for subsequent osteogenic differentiation.[46]

Bone formation primarily occurs in three stages: osteoblast proliferation, extracellular matrix maturation, and mineralization. During these stages, the expression of genes such as ALP, COL-1, Runx2, and OPN plays a crucial role in osteogenic differentiation. ALP (alkaline phosphatase), an important marker of early osteoblast differentiation, is primarily responsible for promoting extracellular matrix mineralization. In the osteoblast differentiation process, ALP expression levels are typically closely associated with cell proliferation and maturation. High ALP expression indicates that osteoblasts have initiated organic matrix secretion and are preparing for subsequent mineralization.[47] Runx2, a key transcription factor for osteogenic differentiation, primarily regulates the expression of osteogenic genes, including ALP and COL-I. The expression of Runx2 plays a priming role in the early stages of osteoblast differentiation, serving as one of the driving factors for bone formation.[48] COL-I (collagen type I), a major component of the bone matrix, plays a pivotal role in boneogenesis. The production of COL-I is closely associated with osteoblast differentiation, mineralization, and bone matrix deposition.[49] OPN (osteopontin), a key protein promoting both bone resorption and mineralization, exerts a dual role in bone remodeling, typically acting in the late stage of osteogenic differentiation.[50] In this study, we found that the gene expression of ALP, Runx2, Col-1, and OPN at the mRNA level in the piezoelectric group was significantly higher than that in the non-piezoelectric group after 7 days, indicating that the combined application of the scaffold and low-intensity pulsed ultrasound (LIPUS) facilitates osteoblast differentiation. Specifically, LIPUS activates the piezoelectric effect of the BT/PLA scaffold to promote bone tissue regeneration, which is consistent with previous findings.[45]

To validate the above in vitro results, we established a rat critical-sized bone defect model to evaluate the in vivo osteogenic capacity of the scaffolds. Eight weeks after scaffold implantation, Micro-CT analysis showed that the blank group exhibited only minimal new bone formation at the defect margin with extremely low bone thickness, confirming successful establishment of the critical calvarial defect model. New bone formation on the surfaces of PLA, PLA+LIPUS, and BT/PLA scaffolds was comparable, whereas the pores of BT/PLA+LIPUS scaffolds were nearly completely filled with new bone and showed higher bone mineral density (BMD), demonstrating the superior bone regenerative capacity of the piezoelectric effect. Moreover, histological staining analysis of hard tissue sections from the samples revealed no inflammatory reactions or pathological abnormalities in any group. Compared with PLA scaffolds, BT/PLA scaffolds showed minimal fibrous connective tissue and new bone formation. In contrast, BT/PLA + LIPUS scaffolds exhibited superior osteogenic capacity, with the scaffold almost entirely covered by new bone and fibrous tissue. These histological staining results were consistent with the Micro-CT findings, indicating that the combination of BT and LIPUS further enhances osteogenesis, which aligns with our in vitro results and existing literature.[51]

Studies have shown that piezoelectric scaffolds, under the action of LIPUS, provide a sustained electrical microenvironment in vivo, where the stable surface potential facilitates rapid and extensive healing of bone defects.[52] Specifically, the electric field effect may influence intracellular components such as ions, growth factors, and receptors, or indirectly affect the extracellular environment via ion/protein aggregation or conformational changes.[53] However, the specific mechanisms remain undefined and warrant further investigation.

Finally, to preliminarily explore and predict the osteogenic mechanism of the 4D bionic piezoelectric scaffold, we conducted transcriptome sequencing. As shown in Figure 8, compared to the PLA + LIPUS group, the BT/PLA+LIPUS group had 326 differentially expressed genes. Enrichment analysis of these genes revealed their significant involvement in the PI3K-Akt signaling pathway, as well as in biological processes related to cell differentiation. Recent studies have demonstrated a growing amount of evidence emphasizing the role of the PI3K-Akt signaling pathway in regulating the self-renewal and differentiation of stem cells.[54] Through qPCR analysis, we observed that the gene expression of PI3K and Akt in the BT/PLA + LIPUS group was significantly upregulated compared to the BT/PLA group, indicating that the piezoelectric effect

activates the PI3K-Akt pathway. Furthermore, after treatment with the PI3K-Akt pathway inhibitor LY294002, we found a significant downregulation of PI3K and Akt expression in the BT/PLA + LIPUS group compared to the same group without the inhibitor, further confirming the impact of the piezoelectric effect on BMSC osteogenic differentiation. Based on these findings, we propose that the mechanism through which the piezoelectric effect promotes osteogenesis might be associated with the stimulation of the PI3K-Akt signaling pathway. The PI3K-Akt pathway is a well-established osteogenic differentiation signaling pathway, consistent with findings reported by Tan et al[55,56] Therefore, we hypothesize that the electrical charges generated by the piezoelectric material create a favorable microenvironment for cell survival, and may promote osteogenic differentiation of BMSCs through the PI3K-Akt pathway. It has been proposed that the piezoelectric effect activates the Piezo1 channel, leading to activation of the PI3K/Akt pathway and subsequent promotion of osteogenesis.[57,58] Further mechanistic investigations will be conducted to explore this in greater depth.

However, our study still has several limitations: (1) the lack of larger animal models; (2) the absence of in-depth investigations into the upstream and downstream mechanisms of the PI3K-Akt signaling pathway. In future experiments, while deeply exploring the osteogenic mechanism of the piezoelectric effect, we will investigate the in vivo angiogenic effect, long-term osteogenic performance, and degradation profile of the scaffold. Simultaneously, we will explore the tripartite interplay among the scaffold, immune modulation, and osteogenesis. Longitudinal in vivo studies and comprehensive safety assessments will be conducted to further validate the efficacy of BT/PLA scaffolds in repairing bone defects under low-intensity pulsed ultrasound (LIPUS) stimulation. Ultimately, these efforts aim to facilitate clinical translation of this technology.

Conclusion

In this study, we successfully fabricated a 20% BT/PLA composite scaffold with dual shape-memory and piezoelectric properties. This design enables the scaffold to not only meet the requirements for minimally invasive implantation but also reconstruct the electrical microenvironment at bone defect sites, establishing it as a novel bioactive scaffold for bone tissue engineering. The scaffold exhibits favorable shape-memory performance, mechanical properties, and piezoelectricity. This composite piezoelectric scaffold not only significantly promotes the adhesion, proliferation, and osteogenic differentiation of bone marrow mesenchymal stem cells (BMSCs) in vitro but also substantially enhances osteogenesis in vivo. In comparison to previous studies, most researchers have solely focused on the impact of single scaffold properties on bone repair. This study breaks new ground by exploring the synergistic effects of composite properties, thereby providing a novel research direction for bone repair scaffolds.

We intend to carry out extended long-term animal experiments to deeply investigate the scaffold's long-term osteogenic performance and degradation behavior in vivo. Simultaneously, we will further optimize the scaffold's performance parameters to better meet the needs of clinical bone repair. Furthermore, we will explore the application potential of this composite scaffold in repairing different types of bone defects, promoting its clinical translation, and bringing more effective therapeutic approaches to patients with bone diseases.

Ethical Statement

All animal experiments were conducted in accordance with the National Institutes of Health (NIH) Guide for the Care and Use of Laboratory Animals and approved by the Ethics Committee of Harbin Medical University (Approval No. YJSDW2023-175). Efforts were made to minimize animal suffering and reduce the number of animals used, following the ARRIVE guidelines (Animal Research: Reporting of In Vivo Experiments).

Acknowledgment

This paper has been uploaded to ResearchGate as a preprint: [https://www.researchgate.net/publication/386473115_Biomimetic_Barium_TitanatePLA_Scaffold_with_Shape_Memory_and_Bioelectro-Active_Capacities_Promotes_Bone_Regeneration].

Author Contributions

All authors made a significant contribution to the work reported, whether that is in the conception, study design, execution, acquisition of data, analysis and interpretation, or in all these areas; took part in drafting, revising or critically reviewing the article; gave final approval of the version to be published; have agreed on the journal to which the article has been submitted; and agree to be accountable for all aspects of the work.

Funding

This work was supported by the National Natural Science Foundation of China (82072472, U23A20412); the Science and Technology Program of the Educational Commission of Heilongjiang Province (31031240043); and Natural Science Foundation of Heilongjiang Province (LH2022H019, LH2021H029, ZD2020H003, JQ2024H003, PL2024H093).

Disclosure

The authors declare that there are no conflicts of interest in this work.

References

1. Guo X, Song P, Li F, et al. Research progress of design drugs and composite biomaterials in bone tissue engineering. *Int J Nanomed*. 2023;18:3595–3622. doi:10.2147/IJN.S415666
2. Zhang X, Li Q, Li L, et al. Bioinspired mild photothermal effect-reinforced multifunctional fiber scaffolds promote bone regeneration. *ACS Nano*. 2023;17(7):6466–6479. doi:10.1021/acsnano.2c11486
3. Eichholz KF, Pitacco P, Burdis R, et al. Integrating melt electrowriting and fused deposition modeling to fabricate hybrid scaffolds supportive of accelerated bone regeneration. *Adv Healthc Mater*. 2024;13(3):e2302057. doi:10.1002/adhm.202302057
4. Resende RF, Fernandes GV, Santos SR, et al. Long-term biocompatibility evaluation of 0.5 % zinc containing hydroxyapatite in rabbits. *J Mater Sci Mater Med*. 2013;24(6):1455–1463. doi:10.1007/s10856-013-4865-x
5. Yassuda-Mattos DH, De Freitas Costa NM, Tavares DDS, et al. Study of bone repair in rat dental socket after implantation of porous granules of beta-tricalcium phosphate (β-TCP) and magnesium-substituted beta-tricalcium phosphate (β-TCMP). *Key Eng Mater*. 2011;493-494:263–268. doi:10.4028/www.scientific.net/KEM.493-494.263
6. Valiense H, Fernandes GVO, Moura B, Calasans-Maia J. Effect of carbonate-apatite on bone repair in non-critical size defect of rat calvaria. *Key Eng Mater*. 2011;493-494:258–262. doi:10.4028/www.scientific.net/KEM.493-494.258
7. Mendes AX, Do Nascimento AT, Duchi S, et al. The impact of electrical stimulation protocols on neuronal cell survival and proliferation using cell-laden GelMA/graphene oxide hydrogels. *J Mater Chem B*. 2023;11(3):581–593. doi:10.1039/D2TB02387C
8. Heng W, Bhavsar M, Han Z, Barker JH. Effects of electrical stimulation on stem cells. *Curr Stem Cell Res Ther*. 2020;15(5):441–448. doi:10.2174/1574888X15666200129154747
9. Khaw JS, Xue R, Cassidy NJ, Cartmell SH. Electrical stimulation of titanium to promote stem cell orientation, elongation and osteogenesis. *Acta Biomater*. 2022;139:204–217. doi:10.1016/j.actbio.2021.08.010
10. Khare D, Basu B, Dubey AK. Electrical stimulation and piezoelectric biomaterials for bone tissue engineering applications. *Biomaterials*. 2020;258:120280. doi:10.1016/j.biomaterials.2020.120280
11. Joo S, Gwon Y, Kim S, Park S, Kim J, Hong S. Piezoelectrically and topographically engineered scaffolds for accelerating bone regeneration. *ACS Appl Mater Interfaces*. 2024;16(2):1999–2011. doi:10.1021/acsami.3c12575
12. Hu ZC, Lu JQ, Zhang TW, et al. Piezoresistive MXene/Silk fibroin nanocomposite hydrogel for accelerating bone regeneration by re-establishing electrical microenvironment. *Bioact Mater*. 2022;22:1–17. doi:10.1016/j.bioactmat.2022.08.025
13. Xu J, Jia Y, Huang W, et al. Non-contact electrical stimulation as an effective means to promote wound healing. *Bioelectrochemistry*. 2022;146:108108. doi:10.1016/j.bioelechem.2022.108108
14. Bhaskar N, Basu B. Osteogenesis, hemocompatibility, and foreign body response of polyvinylidene difluoride-based composite reinforced with carbonaceous filler and higher volume of piezoelectric ceramic phase. *Biomaterials*. 2023;297:122100. doi:10.1016/j.biomaterials.2023.122100
15. Ehterami A, Kazemi M, Nazari B, Saraeian P, Azami M. Fabrication and characterization of highly porous barium titanate based scaffold coated by Gel/HA nanocomposite with high piezoelectric coefficient for bone tissue engineering applications. *J Mech Behav Biomed Mater*. 2018;79:195–202. doi:10.1016/j.jmbbm.2017.12.034
16. Tang Y, Wu C, Wu Z, Hu L, Zhang W, Zhao K. Fabrication and in vitro biological properties of piezoelectric bioceramics for bone regeneration. *Sci Rep*. 2017;7:43360. doi:10.1038/srep43360
17. Chen J, Li S, Jiao Y, et al. In vitro study on the piezodynamic therapy with a batio3-coating titanium scaffold under low-intensity pulsed ultrasound stimulation. *ACS Appl Mater Interfaces*. 2021;13(41):49542–49555. doi:10.1021/acsami.1c15611
18. Lv H, Wang P, Lv Y, et al. Piezo-photocatalytic degradation of ciprofloxacin based on flexible BiVO4 PVDF nanofibers membrane. *Catalysts*. 2025;15(2):163. doi:10.3390/catal15020163
19. Choi SW, Choi WJ, Kim EH, et al. Inflammatory bone resorption and antiosteosarcoma potentials of zinc ion sustained release ZnO chips: friend or foe? *ACS Biomater Sci Eng*. 2016;2(4):494–500. doi:10.1021/acsbiomaterials.5b00395
20. Liu W, Li X, Jiao Y, et al. Dimensionally printed Ti_6Al_4V scaffold coated with piezoelectric $BaTiO_3$ nanoparticles on bone formation. *ACS Appl Mater Interfaces*. 2020;12(46):51885–51903. doi:10.1021/acsami.0c10957
21. Mancuso E, Shah L, Jindal S, et al. Additively manufactured $BaTiO_3$ composite scaffolds: a novel strategy for load bearing bone tissue engineering applications. *Mater Sci Eng C Mater Biol Appl*. 2021;126:112192. doi:10.1016/j.msec.2021.112192

22. Dai X, Yao X, Zhang W, et al. The osteogenic role of barium titanate/polylactic acid piezoelectric composite membranes as guiding membranes for bone tissue regeneration. *Int J Nanomed*. 2022;17:4339–4353. doi:10.2147/IJN.S378422
23. Fan B, Guo Z, Li X, et al. Electroactive barium titanate coated titanium scaffold improves osteogenesis and osseointegration with low-intensity pulsed ultrasound for large segmental bone defects. *Bioact Mater*. 2020;5(4):1087–1101. doi:10.1016/j.bioactmat.2020.07.001
24. Shuai C, Liu G, Yang Y, et al. Functionalized $BaTiO_3$ enhances piezoelectric effect towards cell response of bone scaffold. *Colloids Surf B Biointerfaces*. 2020;185:110587. doi:10.1016/j.colsurfb.2019.110587
25. Pfau MR, McKinzey KG, Roth AA, Graul LM, Maitland DJ, Grunlan MA. Shape memory polymer (SMP) scaffolds with improved self-fitting properties. *J Mater Chem B*. 2021;9(18):3826–3837. doi:10.1039/D0TB02987D
26. Du R, Zhao B, Luo K, et al. Shape Memory polyester scaffold promotes bone defect repair through enhanced osteogenic ability and mechanical stability. *ACS Appl Mater Interfaces*. 2023;15(36):42930–42941. doi:10.1021/acsami.3c06902
27. Zhao W, Yue C, Liu L, Liu Y, Leng J. Research progress of shape memory polymer and 4D printing in biomedical application. *Adv Healthc Mater*. 2023;12(16):e2201975. doi:10.1002/adhm.202201975
28. Zheng T, Pang Y, Zhang D, et al. Integrated piezoelectric/conductive composite cryogel creates electroactive microenvironment for enhanced bone regeneration. *Adv Healthc Mater*. 2023;12(26):e2300927. doi:10.1002/adhm.202300927
29. Sun L, Chen X, Ma K, et al. Novel titanium implant: a 3D multifunction architecture with charge-trapping and piezoelectric self-stimulation. *Adv Healthc Mater*. 2023;12(11):e2202620. doi:10.1002/adhm.202202620
30. Liu J, Li X, Zhang D, et al. Acceleration of bone defect healing and regeneration by low-intensity ultrasound radiation force in a rat tibial model. *Ultrasound Med Biol*. 2018;44(12):2646–2654. doi:10.1016/j.ultrasmedbio.2018.08.002
31. Liu X, Hu Y, Wu L, Li S. Effects of collimated and focused low-intensity pulsed ultrasound stimulation on the mandible repair in rabbits. *Ann Transl Med*. 2020;8(4):98. doi:10.21037/atm.2019.12.89
32. Liu C, Yu B, Zhang Z, et al. LIPUS activated piezoelectric pPLLA/$SrSiO_3$ composite scaffold promotes osteochondral regeneration through P2RX1 mediated Ca^{2+} signaling pathway. *Biomaterials*. 2025;317:123084. doi:10.1016/j.biomaterials.2025.123084
33. Yuan X, Shi J, Kang Y, Dong J, Pei Z, Ji X. Piezoelectricity, pyroelectricity, and ferroelectricity in biomaterials and biomedical applications. *Adv Mater*. 2024;36(3):e2308726. doi:10.1002/adma.202308726
34. Bassett CA. Biologic significance of piezoelectricity. *Calcif Tissue Res*. 1968;1(4):252–272. doi:10.1007/BF02008098
35. Sun K, Luo J, Guo J, Yao X, Jing X, Guo F. The PI3K/AKT/mTOR signaling pathway in osteoarthritis: a narrative review. *Osteoarthritis Cartilage*. 2020;28(4):400–409. doi:10.1016/j.joca.2020.02.027
36. Hou J, Xiao Z, Liu Z, et al. An amorphous peri-implant ligament with combined osteointegration and energy-dissipation. *Adv Mater*. 2021;33(45):e2103727. doi:10.1002/adma.202103727
37. Wu H, Dong H, Tang Z, et al. Electrical stimulation of piezoelectric $BaTiO_3$ coated Ti_6Al_4V scaffolds promotes anti-inflammatory polarization of macrophages and bone repair via MAPK/JNK inhibition and OXPHOS activation. *Biomaterials*. 2023;293:121990. doi:10.1016/j.biomaterials.2022.121990
38. Lai J, Liu Y, Lu G, et al. 4D bioprinting of programmed dynamic tissues. *Bioact Mater*. 2024;37:348–377. doi:10.1016/j.bioactmat.2024.03.033
39. Kenry Liu B, Liu B. Recent advances in biodegradable conducting polymers and their biomedical applications. *Biomacromolecules*. 2018;19(6):1783–1803. doi:10.1021/acs.biomac.8b00275
40. Cai K, Jiao Y, Quan Q, Hao Y, Liu J, Wu L. Improved activity of MC_3T_3-E_1 cells by the exciting piezoelectric $BaTiO_3$/TC_4 using low-intensity pulsed ultrasound. *Bioact Mater*. 2021;6(11):4073–4082. doi:10.1016/j.bioactmat.2021.04.016
41. Bayram C, Demirbilek M, Calişkan N, Demirbilek ME, Denkbaş EB. Osteoblast activity on anodized titania nanotubes: effect of simulated body fluid soaking time. *J Biomed Nanotechnol*. 2012;8(3):482–490. doi:10.1166/jbn.2012.1391
42. Costa DO, Prowse PDH, Chrones T, et al. The differential regulation of osteoblast and osteoclast activity by surface topography of hydroxyapatite coatings. *Biomaterials*. 2013;34(30):7215. doi:10.1016/j.biomaterials.2013.06.014
43. Deligianni DD, Katsala N, Ladas S, Sotiropoulou D, Amedee J, Missirlis YF. Effect of surface roughness of the titanium alloy Ti-6Al-4V on human bone marrow cell response and on protein adsorption. *Biomaterials*. 2001;22(11):1241–1251. doi:10.1016/S0142-9612(00)00274-X
44. Li Z, Qu Y, Zhang X, Yang B. Bioactive nano-titania ceramics with biomechanical compatibility prepared by doping with piezoelectric BaTiO(3). *Acta Biomater*. 2009;5(6):2189–2195. doi:10.1016/j.actbio.2009.02.013
45. Ciofani G, Danti S, Moscato S, et al. Preparation of stable dispersion of barium titanate nanoparticles: potential applications in biomedicine. *Colloids Surf B Biointerfaces*. 2010;76(2):535–543. doi:10.1016/j.colsurfb.2009.12.015
46. Zhou Z, Li W, He T, Qian L, Tan G, Ning C. Polarization of an electroactive functional film on titanium for inducing osteogenic differentiation. *Sci Rep*. 2016;6:35512. doi:10.1038/srep35512
47. Makris K, Mousa C, Cavalier E. Alkaline phosphatases: biochemistry, functions, and measurement. *Calcif Tissue Int*. 2023;112(2):233–242. doi:10.1007/s00223-022-01048-x
48. Chan WCW, Tan Z, To MKT, Chan D. Regulation and role of transcription factors in osteogenesis. *Int J Mol Sci*. 2021;22(11):5445. doi:10.3390/ijms22115445
49. Huang L, Wang J, Yu J, et al. Picein alleviates oxidative stress and promotes bone regeneration in osteoporotic bone defect by inhibiting ferroptosis via Nrf2/HO-1/GPX4 pathway. *Environ Toxicol*. 2024;39(7):4066–4085. doi:10.1002/tox.24239
50. Singh A, Gill G, Kaur H, Amhmed M, Jakhu H. Role of osteopontin in bone remodeling and orthodontic tooth movement: a review. *Prog Orthod*. 2018;19(1):18. doi:10.1186/s40510-018-0216-2
51. Rutten S, Nolte PA, Korstjens CM, van Duin MA, Klein-Nulend J. Low-intensity pulsed ultrasound increases bone volume, osteoid thickness and mineral apposition rate in the area of fracture healing in patients with a delayed union of the osteotomized fibula. *Bone*. 2008;43(2):348–354. doi:10.1016/j.bone.2008.04.010
52. Jacob J, More N, Kalia K, Kapusetti G. Piezoelectric smart biomaterials for bone and cartilage tissue engineering. *Inflamm Regen*. 2018;38:2. doi:10.1186/s41232-018-0059-8
53. Li G, Li Z, Min Y, Chen S, Han R, Zhao Z. 3D-printed piezoelectric scaffolds with shape memory polymer for bone regeneration. *Small*. 2023;19(40):e2302927. doi:10.1002/smll.202302927
54. Yang X, Jiang T, Wang Y, Guo L. The role and mechanism of SIRT1 in resveratrol-regulated osteoblast autophagy in osteoporosis rats. *Sci Rep*. 2019;9(1):18424. doi:10.1038/s41598-019-44766-3

55. Tan P, Hua Y, Yuan B, et al. PI3K/AKT/mTOR signaling regulates BCP ceramic-induced osteogenesis. *J Mater Chem B*. 2024;12(31):7591–7603. doi:10.1039/D4TB01335B
56. Zhao SJ, Kong FQ, Jie J, et al. Macrophage MSR1 promotes BMSC osteogenic differentiation and M2-like polarization by activating PI3K/AKT/GSK3β/β-catenin pathway. *Theranostics*. 2020;10(1):17–35. doi:10.7150/thno.36930
57. Gan D, Tao C, Jin X, et al. Piezo1 activation accelerates osteoarthritis progression and the targeted therapy effect of artemisinin. *J Adv Res*. 2024;62:105–117. doi:10.1016/j.jare.2023.09.040
58. Zhan H, Xie D, Yan Z, et al. Fluid shear stress-mediated Piezo1 alleviates osteocyte apoptosis by activating the PI3K/Akt pathway. *Biochem Biophys Res Commun*. 2024;730:150391. doi:10.1016/j.bbrc.2024.150391